Amelioration of Brain Histone Methylopathies by Balancing a Writer-Eraser Duo KMT2A-KDM5C

Christina N. Vallianatos[1], Brynne Raines[2], Robert S. Porter[1], Mike Wu[3], Patricia M. Garay[1], Katie M. Collette[2], Young Ah Seo[4], Yali Dou[5], Katherine Keegan[1], Natalie Tronson[2], and Shigeki Iwase[1]

[1]Department of Human Genetics, Michigan Medicine, University of Michigan, Ann Arbor, MI 48109

[2]Department of Psychology, College of LS&A, University of Michigan, Ann Arbor, MI 48109

[3]Neurodigitech, LLC, San Diego, CA

[4]Department of Nutritional Sciences, School of Public Health, University of Michigan, Ann Arbor, MI 48109

[5]Department of Pathology, Michigan Medicine, University of Michigan, Ann Arbor, MI 48109

Please address correspondence to: siwase@umich.edu and ntronson@umich.edu

Abstract

Methylation of histone H3 lysine 4 (H3K4me) is extensively regulated by seven writer- and six eraser enzymes in mammalian cells. Nine of the 13 H3K4me enzymes have been associated with neurodevelopmental disorders to date, indicating their important yet poorly-understood roles in the brain. Opposite activities of writer-eraser enzymes highlight modulation of their activities as a therapeutic strategy. However, interplay among the H3K4me enzymes in the brain remains largely unknown. Here, we show functional interactions of a writer-eraser duo, *KMT2A* and *KDM5C*, which are responsible for Wiedemann-Steiner Syndrome (WDSTS), and mental retardation X-linked syndromic Claes-Jensen type (MRXSCJ), respectively. Despite the opposing enzymatic activities, the WDSTS and MRXSCJ mouse models, deficient for either *Kmt2a* or *Kdm5c*, shared similar brain transcriptomes, reduced dendritic spines, and increased aggression. The altered H3K4me landscapes and transcriptomes in the single mutants were partially corrected in the *Kmt2a-Kdm5c* double-mutant (DM) mice. Moreover, the reduced spine density and key behavioral traits including aggression were clearly reversed in DM mice. Thus, our study uncovers common yet mutually-suppressive aspects of WDSTS and MRXCJ and provides a proof of principle for balancing a single writer-eraser pair to ameliorate their associated disorders.

Introduction

Dysregulation of histone methylation has emerged as a major contributor of neurodevelopmental disorders (NDDs) such as autism spectrum disorder and intellectual disability (1-3). Histone methylation can be placed on a subset of lysines and arginines by histone methyltransferases (writer enzymes) and serves as a signaling platform for a variety of nuclear events including transcription (4). Reader proteins specifically recognize methylated histones, thereby converting methylation signals into higher-order chromatin structures (5). Histone methylations can be removed by a set of histone demethylases (eraser enzymes) (6). All three classes of methyl-histone regulators are heavily mutated in NDDs, indicating critical, yet poorly-understood, roles of histone methylation dynamics in brain development and function (7-9).

Histone H3 lysine 4 methylation (H3K4me) is one of the most well-characterized histone modifications. H3K4me is primarily found at transcriptionally active areas of the genome. The three states, mono-, di-, and tri-methylation (H3K4me1-3), uniquely mark gene regulatory elements and play pivotal roles in distinct steps of transcription. While H3K4me3/2 are enriched at transcriptionally-engaged promoters, H3K4me1 is a hallmark of transcriptional enhancers (10, 11). At promoters, H3K4me3 contributes to recruitment of general transcription machinery TFIID and RNA polymerase II (12, 13). H3K4me1 has been shown to tether BAF, an ATP-dependent chromatin remodeling complex, at enhancers (14).

H3K4me is extensively regulated by seven methyltransferases and six demethylases in mammals (6). Consistent with the important roles of H3K4me in transcriptional regulation, genomic distribution of H3K4me appears highly dynamic during brain development (15), in which widespread gene expression changes take place. Developmental H3K4me dynamics appears to be altered in the prefrontal cortices of individuals with autism (16, 17). However, contributions of each of the 13 enzymes in the dynamic H3K4me landscapes of the developing brain remains largely unknown. Strikingly, genetic alterations in nine of the 13 H3K4me enzymes and at least two H3K4me readers have been associated with human NDDs to date, indicating critical roles of H3K4me balance (18) (Figure 1A). These human conditions can be collectively referred to as brain H3K4 methylopathies and point to non-redundant yet poorly-understood roles of these genes controlling this single post-translational modification for faithful brain development.

As histone modifications are reversible, one can, in theory, correct an imbalance by modulating the writers or erasers. Chemical inhibitors of histone deacetylases (HDACs) have been successfully used to rescue phenotypes in mouse models of NDDs. HDAC inhibitors were able to ameliorate learning disabilities in mouse models of Rubinstein-Taybi and Kabuki syndromes, which are deficient for CREBBP or KMT2D, writer enzymes for histone acetylation or H3K4me, respectively (19, 20). However, none of these chemical compounds has yet been proven applicable to human NDDs. Moreover, the HDAC inhibitors such as SAHA and AR-42 used in these studies interfere with multiple HDACs (21), which could potentially result in widespread side effects. Given

the non-redundant roles of the H3K4me enzymes, a more specific perturbation is desirable.

In order to achieve specific modulation of H3K4me rather than inhibiting multiple histone modifiers in a given NDD, the important first step is to delineate functional relationships between the H3K4 enzymes. In the present work, we focus on a pair of NDD-associated writer/eraser enzymes: KMT2A and KDM5C. Haploinsufficiency of *KMT2A* underlies Weidemann-Steiner Syndrome (WDSTS), characterized by intellectual disability, developmental delay, hypotonia, short stature, and facial dysmorphisms, (22, 23). Loss of KDM5C function defines Mental Retardation, X-linked, syndromic, Claes Jensen type (MRXSCJ), in which individuals display an intellectual disability syndrome with aggression, short stature, hypotonia, and occasionally a co-diagnosis of autism (24-27). Mouse models have provided experimental support for causative impacts of KMT2A and KDM5C deficiencies in impaired cognitive development. Heterozygous *Kmt2a* knockout (KO) mice show compromised fear learning (28) and excitatory-neuron-specific *Kmt2a* deletion similarly led to impaired learning, memory, and anxiety behaviors, as well as altered H3K4me3 distributions and transcriptomes (29, 30). In these studies, however, the social behavior and relevant cellular consequences of *Kmt2a* loss were not examined. *Kdm5c*-knockout (KO) mice mimic many MRXSCJ features, including small body size, aggressive behavior, and reduced social activity and learning (31, 32). *Kdm5c*-KO neurons in the basolateral amygdala exhibit malformation of dendritic arbors and spines along with misregulation of neurodevelopmental genes. However, the functional relationships between KMT2A and KDM5C, e.g. how

deficiencies in opposing enzymatic activities can lead to same learning deficits, remain completely unknown. Additionally, despite the strong association with NDDs, successful modulation of histone methylation to restore normal brain physiology has not been reported in these or any other animal models of histone methylopathies.

In the present work, we tested whether modulating either single H3K4me writer or eraser can ameliorate the neurodevelopmental symptoms observed in the WDSTS and MRXSCJ mouse models. We generated *Kmt2a*-, *Kdm5c*-double mutant (DM) mice, and performed systematic comparisons between wild-type (WT), single mutants, and DM mice. The results detailed below revealed common yet mutually-suppressive traits in the two disease models, thereby providing a binary therapeutic strategy for the two conditions.

Results

KMT2A and KDM5C co-exist broadly in the brain

We first examined expression patterns of KMT2A and KDM5C using publicly-available resources, and found the two genes are broadly expressed throughout brain regions of adult mice and humans (Figure S1) (33-37) (38). *Kmt2a* and *Kdm5c* are expressed at comparable levels in all major excitatory and inhibitory neuron subtypes as well as glia cells in mouse visual cortex (Figure S1A), and also throughout mouse brains (Figure S1B). Consistently, developing and aging human brains express *KMT2A* and *KDM5C* at high, steady levels (Figure S1C). Thus, both writer and eraser are co-expressed across brain cell types, regions, and developmental stages in both human and mouse.

Generation of *Kmt2a-Kdm5c* double-mutant (DM) mice

To test genetic interaction of *Kmt2a* and *Kdm5c in vivo*, we generated *Kmt2a-Kdm5c* double-mutant (DM) mice. Experimental mice were F1 hybrids of the two fully-congenic laboratory mouse strains: 129S1/SvImJ *Kmt2a*$^{+/-}$ males (39) and C57BL/6J *Kdm5c*$^{+/-}$ females (31) (Figure 1B). This cross resulted in the following genotypes of male mice: wildtype (WT); *Kmt2a* heterozygote (*Kmt2a*-HET: *Kmt2a*$^{+/-}$), *Kdm5c* hemizygous knock-out (*Kdm5c*-KO: *Kdm5c*$^{-/y}$), and *Kmt2a-Kdm5c* double-mutant (DM: *Kmt2a*$^{+/-}$, *Kdm5c*$^{-/y}$), thereby allowing us to perform systematic comparison between the WDSTS model (*Kmt2a*-HET), the MRXSCJ model (*Kdm5c*-KO), and their composite (DM).

These mice were born at expected Mendelian ratios of 25% per genotype, demonstrating the DM mice were not synthetic lethal (Figure 1C). Genotypes were confirmed at RNA and DNA levels (Figure S2A-C), and protein level for KDM5C (Figure S2D). Brain anatomy showed no gross deformities in any of the genotypes (Figure S2E). Body weight, during the course of development and in adult, however, was reduced in the two single mutants as well as in DM mice (Figure 1D-E). The weight reduction was slightly more pronounced in DM compared to single mutants ($F(3,82) = 11.76$, $p < 0.001$, One-way ANOVA). Thus, loss of *Kdm5c* and *Kmt2a* heterozygosity both led to growth retardation, which was not corrected but rather slightly exacerbated in DM mice.

Altered H3K4me3 landscapes in WDSTS and MRXSCJ models and rescue effects in DM

H3K4me3 is a reaction product of KMT2A-mediated methylation (40), while a substrate for KDM5C-mediated demethylation (41, 42). We sought to determine the impact of KMT2A- and KDM5C-deficiencies and double mutation on the H3K4me3 landscape within the brain. We chose to examine the amygdala tissue, because it plays crucial roles in social behavior and fear memory, which are impaired in *Kdm5c*-KO mice (31). In Western blot analyses, global H3K4me1-3 levels were not altered dramatically in any mutant (Figure S3A). We thus performed H3K4me3 chromatin immunoprecipitation coupled with deep sequencing (ChIP-seq) to probe local changes genome-wide. To assess the IP specificity, we spiked-in an array of recombinant nucleosomes carrying 15 common methylations along with DNA barcodes appended to the Widom601

nucleosome positioning sequence (43) (see Methods). The two H3K4me3 nucleosomes dominated the Widom601-contining DNA in all IP reactions with negligible signals from other methylation states such as H3K4me1 or H3K4me2 (Figure S3B), demonstrating a superb specificity of the ChIP-seq.

To obtain a global picture of H3K4me changes, we examined the H3K4me3 signals between WT and the three mutants throughout the mouse genome partitioned into 1-kilobase (kb) bins (Figure 2A). We found an overall similarity in H3K4me3 coverage across *Kmt2a*-HET, *Kdm5c*-KO, and DM on a genome-wide scale, as well as at promoter regions (Figure 2A, Figure S3C). We then broke down the genome into promoter (± 1 kb from transcription start sites [TSS]), intergenic (between genes), and intragenic (within a gene) regions, and asked if any areas are preferentially dysregulated in any of the mutant animals. In WT, 61% of H3K4me3 fell within promoters, consistent with H3K4me3 as a hallmark of promoters (11-13), while smaller fractions, 18% and 21%, were found in intergenic or intragenic regions, respectively (Figure S3D). This H3K4me3 distribution pattern was largely consistent across the other genotypes (Figure S3D), except for *Kdm5c*-KO and DM amygdala which had slightly higher proportions of intragenic (25% for both) and intergenic (30% and 29%, respectively) methylation (Figure S3D).

Examining local differentially-methylated regions (DMRs), i.e. either hyper- or hypo-methylated for H3K4me3 compared to WT, we found fewer DMRs in *Kmt2a*-HET (1,940) than in *Kdm5c*-KO (11,990) (Figure 2B-G, Figure S3E-H). This difference is

likely due to the heterozygosity of *Kmt2a* which leaves one functional copy of *Kmt2a,* versus the complete loss of *Kdm5c*. Consistently, complete loss of *Kmt2a* in hippocampal neuronal nuclei was previously shown to reduce H3K4me3 in more than four thousand loci (30). In the *Kmt2a*-HET amygdala, hypermethylated loci were primarily found at intragenic regions (56%), while hypomethylated regions were found mainly at promoters (76%, Figure 2C). *Kdm5c*-KO DMRs were biased towards an increase in methylation signals (8,284 hypermethylated vs. 3,706 hypomethylated), consistent with loss of a demethylase. In the *Kdm5c*-KO amygdala, the hypermethylated loci showed a roughly even split between promoters, intragenic, and intergenic regions, while the majority of the *Kdm5c*-KO hypomethylated regions were located at promoters (89%, Figure 2F). Hypermethylation in non-promoter regions was also detected as an appearance of additional H3K4me3 peaks in *Kdm5c*-KO amygdala (Figure S3D). When we overlapped single mutant DMRs (Figure 2H), most DMRs were unique to *Kdm5c*-KO (10,994). Interestingly, one half of the *Kmt2a*-HET DMRs overlapped with *Kdm5c*-DMRs (Figure 2H), and these DMRs were misregulated in the same direction between the two single mutants (Figure 2I), despite the opposing activity of this pair of enzymes. Motif analysis identified distinct as well as common transcription factor-binding motifs at *Kmt2a*-HET and *Kdm5c*-KO DMRs (Figure SI-J). Thus, *Kmt2a*- and *Kdm5c*-deficiencies lead to both unique and common alterations in H3K4me3 landscapes.

We next asked if any of these DMRs were corrected in double mutants (DM). We defined “rescued” regions as DMRs identified in single mutants that were no longer categorized as a DMR in DM (therefore, no different from WT). We observed a rescue

of roughly half of single mutant DMRs in our DM animals: 42% (821/1,940) of *Kmt2a*-HET DMRs and 54% (6,576/11,990) of *Kdm5c*-KO DMRs became non-DMR states in DM (Figures 2D, 2G, S3E-H). Representative examples of rescued and unrescued DMRs are shown (Figure 2J-M).

Most rescued DMRs show smaller yet detectable fold changes of H3K4me3 in DM, indicating that the rescue effect was partial (Figure 2N). If KMT2A and KDM5C simply counteract, we should observe that hypermethylated regions in *Kdm5c*-KO are hypomethylated in *Kmt2a*-HET, and normalized in DM. We indeed observed such cases in a small fraction of rescued DMRs (solid bars in Figure 2N). Unexpectedly, some regions showed reciprocal H3K4me3 changes between the single mutants in an opposite way as expected; namely, hypomethylation in *Kdm5c*-KO and hypermethylation in *Kmt2a*-HET (open bars in Figure 2N). The most prevalent pattern of rescued DMRs was the hypermethylated regions of *Kdm5c*-KO that were still moderately hypermethylated in DMs and unexpectedly in *Kmt2a*-HET as well (striped bars in Figure 2N). Thus, simple counteractions between *Kmt2a* and *Kdm5c* are relatively rare events, and rather deficiency of the single enzyme results in a complex change of H3K4me3 homeostasis. Nonetheless, our analyses identified thousands of genomic loci at which KMT2A and KDM5C fully or partially mediate aberrant H3K4me3 levels caused by loss of the opposing enzyme.

Transcriptomic similarity between WDSTS and MRXSCJ models and rescue effects in DM

We previously showed *Kdm5c*-KO mice exhibit aberrant gene expression patterns in the amygdala and frontal cortex (31), and the hippocampus (32). Excitatory-neuron specific conditional *Kmt2a*-KO mice were also characterized with altered transcriptomes in the hippocampus and cortex (29, 30). However, the global gene expression of *Kmt2a*-HET, which is akin to the WDSTS syndrome genotypes, has not been determined. To compare the impact of *Kmt2a*-haploinsufficiency and *Kdm5c*-KO on the transcriptome, we performed unique molecular identifiers (UMI)-RNA-seq (44) using amygdala tissues of adult mice across the four genotypes. To minimize the impact of PCR-derived duplication on gene expression analysis, we used primers containing UMIs during library amplification, and deduplicated the sequencing reads prior to analysis (see Methods). First, we confirmed the lack or reduction of reads from *Kdm5c* exons 11 and 12 and *Kmt2a* exons 8 and 9 in the corresponding mutants (Figure S2A-B). Spike-in RNA controls confirmed the broad dynamic range of differential gene expression analysis (Figure S4A). The gene expression changes observed in the *Kdm5c*-KO amygdala were similar between the present dataset and our previous dataset obtained from a different cohort of mice (31), demonstrating the reproducibility of the UMI-RNA-seq approach (Figure S4B).

We identified a similar number of differentially-expressed (DE) genes ($p < 0.01$) in *Kmt2a*-HET (136 genes) and *Kdm5c*-KO (127 genes) compared to WT amygdala, while DM yielded 203 DE genes (Figure 3A). In general, KMT2A acts as a transcriptional coactivator by placing H3K4me (39, 40, 45) and KDM5C primarily suppresses transcription by removing this mark (41), yet roles for KDM5C as a positive regulator of

transcription have also been reported (46, 47). Reminiscent of some H3K4me changes that were similar between the single mutants (Figure 2I and 2N), examination of fold changes of all DE genes pointed to similar transcriptome alterations in all three mutants compared to WT (Figure 3B). Furthermore, a substantial number of DE genes overlap among the three mutants and many of them showed changes in the same direction between single mutants (Figures 3C, S4C-D), while no genes were reciprocally misregulated (Figure 3D). Consistently, the single-mutant DE genes were largely misregulated in the same direction as the other single mutant (Figure S4E-F). With respect to the biological implications of the gene misregulation, we did not find any conspicuous alterations of neuronal activity-dependent genes, cell-type specific transcripts, and developmentally-regulated genes in any of the mutant DE genes (Figure S5).

Next, we sought to test if normal expression of any individual genes was restored in DM. To this end, we counted single-mutant DE genes that had higher *p*-values than a relaxed significance threshold ($p > 0.1$) in DM vs. WT comparison; an indicator of normal expression. We found that 33% (42/127) of *Kdm5c*-KO-DE genes and 56% (76/136) *Kmt2a*-HET-DE genes were expressed normally in DM (highlight in Figure 3E). The rescue effects were visible when we analyzed all single-mutant DE genes as a group (Figure S4D). To better understand how transcriptomic similarity and rescue effect can occur simultaneously, we plotted expression fold changes of the 118 rescued genes (Figure 3F). We observed that rescued genes were differentially dysregulated in single mutants, e.g. upregulated in *Kdm5c*-KO but unchanged in *Kmt2a*-HET (Figure

3F). Thus, these results indicate that the largely-separate sets of genes contribute to the overall transcriptome similarity and the rescue effect in DM.

Pathway analysis of these 118 rescued genes did not yield statistically-significant enrichment of any pathways, however, we were able to separate rescued genes into specific biological pathways that could potentially be restored in DM (Supplementary Table 1). Notably, genes that have established roles in central nervous system development and are genetically associated with neurodevelopmental disorders were among these restored genes in DM. These genes include *Gnao1* (48, 49), *Bcl11b* (50), *Arnt2* (51), *Mkks* (52-55), *Arid1a* (56), *Rora* (57), and *Sez6* (58).

We then examined the relationship between the H3K4me3 landscape and transcriptome alterations. If H3K4me3 changes drive the gene misregulation in mutants, we should be able to observe a correlation between these two datasets. However, genes with altered promoter-proximal H3K4me3 did not show significant changes in their expression as a group (Figure S6A). While H3K4me3 changes are the direct molecular consequences of KMT2A- and KDM5C-deficiency, the steady-state mRNAs we captured in our RNA-seq approach likely involve indirect and adaptive consequences of loss of these enzyme(s), which can lead to an underwhelming correlation between H3K4me3 and transcriptome data. Indeed, we observed a positive correlation between intergenic H3K4me3 levels and spurious transcripts, which are generated at these regions yet likely unstable, therefore, can reflect transcriptional activity more reliably than steady-state mRNA levels (Figure S6B). Such spurious intergenic transcripts were previously observed in

the *Kdm5c*-KO hippocampus (32). We also examined the H3K4me3 coverage at promoter regions of DE genes (Figure S6C). Across the different DE gene categories, H3K4me3 levels did not differ between genotypes, with two exceptions: *Kmt2a*-HET down-regulated and *Kdm5c*-KO up-regulated genes showed the expected changes in median H3K4me3 levels (Figure S6C). The correlation was also evident between expression of rescued genes and H3K4me3 (Figure S6D). Together, these observations indicate that H3K4me3 changes are not sufficient, yet an important contributor, for gene misregulation in single mutants and its correction in DM.

Shared dendritic phenotypes in *Kmt2a*-HET and *Kdm5c*-KO were reversed in DM

Altered dendrite morphology is a hallmark of many human neurodevelopmental disorders (NDDs), as well as animal models of NDDs (31, 59-62). We previously found that reduced dendritic length and spine density in basolateral amygdala (BLA) neurons of *Kdm5c*-KO adult male mice (31). Assessment of dendritic morphology in *Kmt2a*-HET has not been reported. We performed comparative dendrite morphometry of pyramidal neurons in the BLA using Golgi staining for the four genotypes (Figure 4). For *Kdm5c*-KO neurons, we recapitulated our previous findings of reduced dendrite lengths (Figure 4B) ($F(3,89) = 2.776$; $p = 0.0459$; WT vs. *Kdm5c*-KO: $p = 0.0341$, one-way ANOVA followed by Tukey multiple comparison tests) and lower spine density (Figure 4C) ($F(3,89) = 82.25$; $p < 0.0001$; WT vs. *Kdm5c*-KO: $p = 0.0079$). *Kmt2a*-HET neurons looked remarkably similar to *Kdm5c*-KO (Figure 4A), exhibiting trends of reduction in dendrite length, which was not significantly different than WT, however, was also not different than *Kdm5c*-KO (Figure 4B) (WT vs. *Kmt2a*-HET: $p = 0.1772$; *Kdm5c*-KO vs.

Kmt2a-HET $p = 0.8906$). Similarly, spine densities of *Kmt2a*-HET neurons were significantly lower compared to WT and not significantly different than *Kdm5c*-KO (Figure 4C) (WT vs. *Kmt2a*-HET: $p = 0.0053$; *Kdm5c*-KO vs. *Kmt2a*-HET $p = 0.9993$). Loss of both *Kmt2a* and *Kdm5c* together had an overall positive effect on neuron morphology (Figure 4A). DM dendrite lengths showed trends of restoration (Figure 4B), as they were not significantly different than WT (WT vs. DM: $p = 0.5503$), however were also not different than *Kdm5c*-KO (*Kdm5c*-KO vs. DM: $p = 0.5341$). DM exhibited an increase in dendritic spine density that surpassed a rescue effect (Figure 4C) (WT vs. DM: $p < 0.0001$; *Kdm5c*-KO vs. DM: $p < 0.0001$, *Kmt2a*-HET vs. DM: $p < 0.0001$). As morphology of dendritic spines progressively changes during synaptogenesis and development (63), we also asked whether developmental subtypes of dendritic spines were altered in any genotype. We did not find dramatic changes in spine morphology among the four genotypes (Figure 4D), indicating selective requirement of *Kdm5c* and *Kmt2a* for regulation of spine numbers, but not for morphology. Overall, we conclude that *Kmt2a*-HET and *Kdm5c*-KO share similar dendritic morphology deficits, which are reversed in DM.

Memory alterations in *Kdm5c*-KO were reversed in DM

After observing the restorative molecular and cellular effects in DM mice, we next sought to determine the effect of loss of *Kmt2a* and/or *Kdm5c* on mouse behaviors through a battery of behavioral tests. In accordance with previous findings (31, 32), *Kdm5c*-KO mice showed significant deficits in associative fear memory, as measured by the contextual fear conditioning (CFC) tests (Figure 5A) ($F(3,64) = 2.83$, $p = 0.046$; WT

vs. *Kdm5c*-KO: $p = 0.018$). In the novel object recognition tests (NOR), where WT mice showed preference for the new object, *Kdm5c*-KO mice tended to avoid the novel object (Figure 5B) ($F(3,64) = 3.20$, $p = 0.030$; WT vs. *Kdm5c*-KO: $p = 0.007$). Homozygous deletion of *Kmt2a* in excitatory hippocampal neurons leads to impaired fear memory in the CFC (30), a hippocampal-dependent memory test (64). In our tests, *Kmt2a*-HET mice showed no deficits compared to WT mice (Figure 5A-B) (CFC: $p = 0.789$; NOR; $p = 0.888$), indicating stronger cognitive deficits in the MRXSCJ model compared to WDSTS model mice. Importantly, DM mice also showed no differences from WT mice (Figure 5A-B) (CFC: $p = 0.246$; NOR: $p = 0.756$), suggesting that *Kmt2a* heterozygosity can rescue memory deficits of *Kdm5c*-KO mice. These differences in memory tasks were not attributable to differences in locomotor activity or shock responsiveness, as none of these parameters showed significant differences among the genotypes (Figure 5C-D).

Social behaviors are differently dysregulated in *Kmt2a*-HET, *Kdm5c*-KO, and DM mice

In the three-chambered social interaction test (Figure 6A), we observed significant differences between genotypes ($F(3,61) = 4.314$, $p < 0.008$). *Kmt2a*-HET mice showed no differences from WT ($p = 0.082$), in accordance with previous tests in conditional *Kmt2a*-KO mice (30). In contrast, *Kdm5c*-KO ($p= 0.002$), as previously shown (31), as well as DM ($p = 0.011$) mice showed significantly less preference for the stranger mouse compared with WT animals. These data suggest that *Kmt2a* heterozygosity does not rescue deficits of social interaction in the *Kdm5c*-KO.

In tests of social dominance (Figure 6B), *Kmt2a*-HET mice won against WTs in 60.9% in of the matches against WT (p = 0.091), and *Kdm5c*-KO mice won at least 68.4% of the time (p = 0.008). Surprisingly, DM animals lost more than 80% of their bouts against WT ($p = 1.47 \times 10^{-5}$). Although DM mice were slightly smaller compared to single mutants (Figure 1D), this is unlikely to drive submissive behaviors, as body mass has been shown to have minimal impact on social hierarchy unless excess difference (> 30%) is present between animals (65-67), which is not the case in our study (Figure 1D) (11% *Kmt2a*-HET vs. WT, 17% *Kdm5c*-KO vs. WT, 25% DM vs. WT). These results demonstrate that a significant increase of social dominance in *Kdm5c*-KO and a similar trend in *Kmt2a*-HET are mediated by opposing enzymes.

In the resident-intruder test, we observed differences in overall aggression between genotypes (Figure 6C) ($F(4,61) = 3.015$, $p = 0.037$), and differences across specific types of aggressive behaviors (Figures 6D-H, S7A-E) ($F(12,61) = 2.15$, $p = 0.015$). Specifically, we found increased darting (Figures 6D, S7A) in both *Kdm5c*-KO (p = 0.006) and *Kmt2a*-HET (p = 0.032) mice together with decreased aggression in DM mice, which showed significantly less mounting (Figures 6E, S7B) (*cf* WT: p =0.072; *cf* *Kdm5c*-KO: p = 0.019; *cf* *Kmt2a*-HET: p = 0.004), and chasing (Figures 6F, S7C) (*cf* WT: p =0.027; *cf* *Kdm5c*-KO: p = 0.010; *cf* *Kmt2a*-HET: p = 0.007) than all other genotypes. Moreover, we also observed an overall effect of genotype on submissive behaviors of resident mice (Figure 6I) ($F(3,61) = 4.071$, $p = 0.011$). For the specific type of submissive behaviors, DM mice exhibited significantly more cowering (Figures 6J,

S7F) compared with all other genotypes (*cf* WT : $p = 0.028$; cf *Kdm5c*-KO: $p = 0.006$; cf *Kmt2a*-HET: $p = 0.005$), and significantly more running away (Figures 6K, S7G) compared with *Kdm5c*-KO ($p = 0.008$). Importantly, the genotype effect on submissive behaviors inversely correlated with that of aggressive behavior, reinforcing the difference in specific behaviors rather than changes in locomotor activity.

Together, the behavioral studies revealed more pronounced deficits of *Kdm5c*-KO animals compared to *Kmt2a*-HET mice on memory and social interaction, while *Kmt2a*-HET and *Kdm5c*-KO mice shared increased social dominance and aggression. The consequences of double mutations varied between the tests, with clear rescue effects on cognitive tasks, dominant behavior, and aggression, and no effect on social interactions. Notably, however, no behavioral traits were exacerbated in DM. These results support the idea that the two enzymes mediate some, if not all, deficiencies caused by writer-eraser imbalance at the behavioral level.

Discussion

The present work represents the first genetic interactions between chromatin modification writer and eraser enzymes *in vivo*, to our knowledge. Discovery of chromatin-modifying enzymes in the past decades made it clear that virtually no DNA- or histone-modifications are irreversible, and instead are subjected to dynamic regulation by writer and eraser enzymes. The genes encoding these enzymes appear to have undergone duplication events during evolution. Complex organisms carry a greater number of genes that encode enzymes for single chromatin modification. For example, only one enzyme, Set1, is responsible for H3K4 methylation in fission yeast. In fly, three genes, *Trx*, *Trr*, and *Set1* mediate H3K4me installation, and all three genes were duplicated in the mammalian genomes, which resulted in six SET-family H3K4 writers (68). A plethora of work has demonstrated specialized as well as redundant roles of individual histone-modifying enzymes within a family, in broad biological processes such as cancer and development (69). A fundamental question remained — is there any specific writer-eraser pairing in such highly-duplicated gene families for a single chromatin modification? Mishra *et al*. showed that KDM5A antagonizes KMT2A, KMT2B, and KMT2D to modulate the transient site-specific DNA copy number gains in immortalized human cells (70). Cao et al. found that failed differentiation of mouse embryonic stem cells due to *Kmt2d* deletion can be rescued by *Kdm1a* knockdown (71). These pioneering efforts identified functional interplay between the opposing enzymes *in vitro*, however, no *in vivo* study has been reported. Thus, the present study

substantially advances our understanding of how methyl-histone writer and eraser enzymes functionally interact during brain development and function.

Brain development is particularly relevant to the H3K4me dynamics, because a cohort of neurodevelopmental disorders have been genetically associated with impaired functions of these enzymes, as discussed earlier. Our work illuminates the similarities between WDSTS and MRXSCJ model mice in gene expression and neuronal morphological levels, although the two conditions are associated with opposing enzymatic activities. Consistently, many symptoms are common between WDSTS and MRXSCJ, including intellectual disability, short stature, seizures, aggressive behavior, and hypotonia (23-25, 72). Thus, our work underscores a shared pathophysiology of the two conditions. Unlike previous studies using chemical approaches that block multiple chromatin regulators (19-21), we demonstrated that manipulation of a single enzyme, KMT2A or KDM5C, is sufficient to reverse many neurological traits. It may not be surprising that not all traits were reversed in DM mice, such as H3K4me3 at specific loci (Figure 2), expression of some genes (Figure 3), and social preference (Figure 6), because remaining H3K4me enzymes may potentially mediate these un-rescued traits. Our work opens a new avenue for future studies to delineate the full interplay between the 13 H3K4me-regulatory enzymes throughout brain development and function.

Increased social dominance is a novel behavioral trait we found in both WDSTS and MRXSCJ mouse models. The amygdala is well known to mediate social behaviors (73, 74). For example, lesions of BLA result in decreased aggression-like behavior and

increased social interactions (75, 76), and changes in transcriptional regulation in BLA are observed after social interactions (74). Decreased dendritic spine density in *Kmt2a*-HET and *Kdm5c*-KO mice inversely correlates with increased social dominance and aggression (Figures 4 and 6), suggesting that decreased spine density does not represent a loss-of-function in the amygdala, and rather, may reflect a loss of inhibitory control over the amygdala. Thus, determining the connectivity of amygdala with other regions, including prelimbic, infralimbic, and orbitofrontal cortices (77) as well as ventral hippocampus (73) will be critical for understanding the changes in social behaviors in both WDSTS and MRXSCJ models.

It is important to note that the double mutations introduced in our mice were constitutive in this study, and therefore a lifetime of adaptation to loss of these two major chromatin regulators may complicate the phenotypes and rescue effects measured. A more realistic therapeutic strategy may be acute inhibition of KDM5C and KMT2A in a developing brain. Previous work characterizing mouse models with excitatory-neuron specific ablation of *Kdm5c* or *Kmt2a* via *CamKII*-Cre found that conditional *Kmt2a* deletion led to clear learning deficits (30), while cognitive impairments in the conditional *Kdm5c*-KO mice were much milder than those of constitutive *Kdm5c*-KO mice (32). These results suggest a developmental origin of phenotypes in *Kdm5c*-KO. Future investigations are needed to address whether the effects of acute inhibition of opposing enzymes in these mouse models can restore such neurodevelopmental deficits.

With any therapeutic intervention, careful assessments of side effects will be inevitable. In our work, while a substantial fraction of H3K4me3 DMRs and gene misregulation in single mutants were corrected in DM (Figures 2 and 3), combinatorial ablation of KMT2A and KDM5C should reduce net regulatory action over H3K4me3, which may lead to adverse consequences. Indeed, our genomics approaches identified H3K4me3 DMRs that are unique to the DM brain, and several genes uniquely misregulated in DM animals (Figure S8). It is still plausible that these gene and H3K4me3 changes in DM can lead to phenotypic outcomes were not examined in this study. Nevertheless, we were encouraged that none of the neurological traits measured in this study showed exacerbation in DM.

Our work provides useful insights into clinical applications aiming to ultimately treat H3K4 methylopathies. While the presented data nominate KMT2A and KDM5C as therapeutic targets to intervene MRXSCJ and WDSTS, we imagine this strategy to identify writer-eraser pairs may be key to developing remedies tailored to specific histone methylopathies.

Materials & Methods

Mouse models

Kdm5c-KO mice were previously described (31). *Kmt2a*-HET mice were generated by crossing previously-described *Kmt2a*-flox (exons 8 and 9) mice with B6.129-Gt(ROSA)26Sor$^{tm1(cre/ERT2)Tyj}$/J-Cre mice (78). To backcross *Kmt2a*$^{+/-}$ mice onto the desired 129S1/SvImJ strain, we employed the marker assisted accelerated backcrossing through Charles River Labs. *Kmt2a*$^{+/-}$ mice were bred to the N4 generation at minimum, where mice were >90% congenic for 129S1/SvImJ. All experimental mice were generated as F1 generation hybrids from mating between 129S1/SvImJ *Kmt2a*$^{+/-}$ males and C57Bl/6 *Kdm5c*$^{+/-}$ females: WT males (*Kmt2a*$^{+/+}$*, Kdm5c*$^{+/y}$); *Kdm5c*-KO males (*Kmt2a*$^{+/+}$*, Kdm5c*$^{-/y}$); *Kmt2a*-HET males (*Kmt2a*$^{+/-}$*, Kdm5c*$^{+/y}$); and *Kdm5c-Kmt2a*-DM males (*Kmt2a*$^{+/-}$*, Kdm5c*$^{-/y}$). Genotypes were confirmed using the following primers: for *Kmt2a*, 5'-GCCAGTCAGTCCGAAAGTAC, 5'-AGGATGTTCAAAGTGCCTGC, 5'-GCTCTAGAACTAGTGGATCCC; for *Kdm5c*, 5'-CAGGTGGCTTACTGTGACATTGATG, 5'-TGGGTTTGAGGGATACTTTAGG, 5'-GGTTCTCAACACTCACATAGTG.

Western blot analysis

Total proteins from adult brain tissues were subjected to Western blot analysis using in-house anti-KDM5C (31), and anti-GAPDH antibodies (G-9, Santa Cruz). For histone proteins, nuclei were enriched from the dounce-homogenized brain tissues using Nuclei EZ prep Kit (Sigma, NUC-101). DNA were digested with micrococcal nuclease (MNase,

NEB) for 10 minutes at room temperature and total nuclear proteins were extracted by boiling the samples with the SDS-PAGE sample buffer. The following antibodies were used for Western blot analyses: anti-H3K4me3 (Abcam, ab8580), anti-H3K4me2 (Thermo, #710796), anti-H3K4me1 (Abcam, ab8895), and anti-H3 C-terminus (Millipore, CS204377).

Brain histology

Mice were subjected to transcardial perfusion according to standard procedures. Fixed brains were sliced on a freeze microtome, yielding 30 μm sections that were then fixed, permeabilized, blocked, and stained with DAPI. Slides were imaged on an Olympus SZX16 microscope, with an Olympus U-HGLGPS fluorescence source and Q Imaging Retiga 6000 camera. Images were captured using Q-Capture Pro 7 software.

ChIP-seq

Brains from adult (6-8 months) male mice were microdissected to enrich for the amygdala. N=2 animals were used for WT, and N=3 animals were used for *Kmt2a*-HET, *Kdm5c*-KO, and DM as biological replicates. Nuclei were isolated using Nuclei EZ prep Kit (Sigma, NUC-101), and counted after Trypan blue staining. 20,000 nuclei for each replicate were subjected to MNase digestion as previously described (79). We essentially followed the native ChIP-seq protocol (79) with two modifications. One was to use a kit to generate sequencing libraries in one-tube reactions (NEB, E7103S). Another modification was to spike-in the panel of synthetic nucleosomes carrying major

histone methylations (EpiCypher, SKU: 19-1001) (43). For ChIP, we used the rabbit monoclonal H3K4me3 antibody (Thermo, clone #RM340).

Libraries were sequenced on the Illumina NextSeq 500 platform, with single-end 75 base-pair sequencing, according to standard procedures. We obtained 20 to 59 million reads per sample. Reads were aligned to the mm10 mouse genome (Gencode) and a custom genome containing the sequences from our standardized, synthetic nucleosomes (EpiCypher) for normalization (80), using Bowtie allowing up to 2 mismatches. Only uniquely-mapped reads were used for analysis. All replicates had a mean of 9.1 million uniquely mapping reads (range: 7.4 to 13.9 million). The enrichment of mapped synthetic spike-in nucleosomes compared to input was calculated and used as a normalization coefficient for read depth each ChIP-seq replicate (80).

Peaks were called using MACS2 software (v 2.1.0.20140616) (81) using input BAM files for normalization, with filters for a q-value < 0.1 and a fold enrichment greater than 1. Differentially-methylated regions (DMRs) were called using the MACS2 bdgdiff command with default parameters and incorporating the synthetic nucleosome normalization into the read depth factor. Bedtools was used to calculate coverage across individual replicates. We also used Bedtools to intersect peaks of interest with mm10 promoters (defined here as ±1 kb from annotated transcription start site [TSS]), intragenic regions (as defined by annotated mm10 gene bodies, but excluding the previously defined promoter region), and intergenic regions (regions that did not overlap with promoters or gene bodies). DMRs from single mutants (2a-HET or 5c-KO) were

considered “rescued” in DM animals if that single-mutant peak was *not* called as a DMR in the DM analysis. For the global H3K4me3 analysis, the Bedtools multicov command was used to calculate coverage over 1 kb windows throughout the genome, as well as at each promoter (±1 kb from annotated TSS). HOMER (v4.10) was used to carry out motif enrichment analysis (82). We selected the top 5 motifs, and only motifs from known mammalian ChIP-seq experiments were represented in our data. Normalized bam files were converted to bigwigs for visualization in the UCSC genome browser. Genes near peaks were identified by Bedtools and RefSeq genomic accession number were converted to official gene symbol using bioDBnet (83).

The ChIP-seq data have been deposited in NCBI’s Gene Expression Omnibus (84). Data are accessible through GEO series accession numbers: SuperSeries GSE127818, SubSeries GSE127817, and can be accessed with secure token *ovuhykuazryxrad*.

RNA-seq

Brains from adult (3 to 6 months) male mice were microdissected to enrich for the amygdala. N=3 animals were used per genotype. Tissue was homogenized in Tri Reagent (Sigma). Samples were subjected to total RNA isolation, and RNA was purified using RNEasy Mini Kit (Qiagen). ERCC spike-in RNA was added at this stage, according to manufacturer’s instructions (Life Technologies). Ribosomal RNA was depleted using NEBNext rRNA Depletion kit (New England Biolabs). Libraries were prepared using the Click-seq method, using primers containing unique molecular

identifiers (UMIs), as described previously (44). Multiplexed libraries were pooled in approximately equimolar ratios and purified using Agencourt RNAClean XP beads (Beckman Coulter).

Libraries were sequenced on the Illumina HiSeq 4000 platform, with paired-end 150 base pair reads, according to standard procedures. Reads were mapped to the mm10 mouse genome (Gencode) using STAR (v2.5.3a) (85), where only uniquely mapped reads were used for downstream analyses. Duplicates were removed using UMI-tools (v0.5.4) (86), and a counts file was generated using FeatureCounts (Subread v1.5.0) (87). BAM files were converted to bigwigs using deeptools (v3.1.3) (88, 89). Differentially expressed (DE) genes were called using DESeq2 (v1.14.1) (90, 91). According to the previous RNA-seq study of *Kdm5c*-KO mice (31), we used $p < 0.01$ to identify DE genes. Data analyses were performed with RStudio (v1.0.136) or GraphPad Prism (v7.00 or 8.02) for Mac (GrapPad Software, La Jolla California USA, www.graphpad.com). Fold change heatmaps was created using shinyheatmap on the web (92). Cell type expression data was downloaded from the Barres lab Brain RNA-seq Portal (93). Cell type enriched genes were determined as having > 5 FPKM in cell type A and > 2 FPKM cell A FPKM/each other cell type FPKM. We identified 471 astrocyte (A), 629 neuron (N), 840 micorglia (M), 197 oligodendrocyte precursor (Op), 74 newly formed oligodendrocyte (On), 96 myelinating oligodendrocyte (Om), and 716 endothelial (E) cell enriched genes. Temporal expression data from human male amygdala was downloaded from the BrainSpan Atlas of Developing Human Brain (94).

The RNA-seq data have been deposited in NCBI's Gene Expression Omnibus (84). Data are accessible through GEO series accession numbers: SuperSeries GSE127818, SubSeries GSE127722, and can be accessed with secure token *ovuhykuazryxrad*.

Golgi staining

Morphological analyses of dendrites were carried out as described previously (95) on adult (2-8 months) mice. Four animals were used for each genotype, and at least 20 pyramidal neurons in the basolateral amygdala per animal were quantified. We examined dendritic lengths, branch patterns, spine counts, spine density, and spine morphology.

Behavioral paradigms

Prior to behavioral testing, mice were acclimated to the animal colony room for one week single-housing in standard cages provided with lab diet and water *ad libitum*. A 12-hour light-dark cycle (7:00AM-7:00PM) was utilized with temperature and humidity maintained at 20 ±2 ºC and >30%, respectively. The University of Michigan Committee on the Use and Care of Animals approved all tests performed in this research. Five tests, listed in order of testing, were performed: Novel Object Recognition (5 days), Context Fear Conditioning (2 days), Three-Chambered Social Interaction (2 days), Social Dominance Tube Test (3-4 days), and Resident-intruder (2-3 days). All testing was conducted in the morning by experimenters blind to genotype. 70% ethanol was used as a cleaning agent in every test between each trial.

Novel Object Recognition: Mice were first habituated to testing arenas (40 x 30 x 32.5 cm^3) in three, 10 minute sessions over six consecutive days (96, 97). 24 hours later, mice were allowed to explore on two identical objects (jar or egg, counterbalanced across animals) for two, 10-minute trials spaced three hours apart. All animals were returned to the arena tested 24 hours after the first training session and presented with one training object ("familiar" object: jar or egg) and one "novel" object (egg or jar). Exploration of the objects was defined as nose-point (sniffing) within 2 cm of the object. Behavior was automatically measured by Ethovision XT9 software using a Euresys Picolo U4H.264No/0 camera (Noldus, Cincinnati, OH). Preference was calculated as the time spent exploring novel object/total time exploring both objects. One-sample t-tests against 50% (no preference) were used to establish whether animals remembered the original objects.

Contextual Fear Conditioning: Context fear conditioning was assessed as previously described (98). Mice were placed into a distinct context with white walls (9 ¾ × 12 ¾ × 9 ¾ in) and a 36 steel rod grid floor (1/8 in diameter; ¼ spaced apart) (Med-Associates, St. Albans, VT) and allowed to explore for 3 minutes, followed by a 2-second 0.8 mA shock, after which mice were immediately returned to their home cages in the colony room. 24 hours later, mice were returned to the context and freezing behavior was assessed with NIR camera (VID-CAM-MONO-2A) and VideoFreeze (MedAssociates, St Albans, VT). Freezing levels were compared between genotypes using a between-groups analysis (one-way ANOVA) with genotype as the between-subjects factor.

Three-Chambered Social Interaction: Mice were placed into a three-chambered apparatus consisting of one central chamber (24 x 20 x 30 cm^3) and two identical side chambers (24.5 x 20 x 30 cm^3) each with a containment enclosure (8 cm diameter; 18 cm height; grey stainless steel grid 3 mm diameter spaced 7.4 mm apart) and allowed to habituate for 10 minutes. 24 hours later, mice were returned to the apparatus that now included a 2-3 month old stranger male mouse (C57BL/6N) on one side of the box ("stranger"), and a toy mouse approximately same size and color as stranger mouse on other ("toy"). Exploration of either the stranger or toy was defined as nose-point (sniffing) within 2 cm of the enclosure and used as a measure of social interaction (99). Behavior was automatically scored by Ethovision XT9 software as described above, and social preference was defined as time exploring stranger/total exploration time. Social preference was analyzed using one-sample t-tests for each genotype. A repeated measures analysis was used for each aggression (genotype x aggression measures ANOVA) and submissive behaviors (genotype x submissive) to analyze aggressive behaviors.

Social Dominance Tube Test: 24 hours prior to testing, mice were habituated to the plastic clear cylindrical tube (1.5 in diameter; 50 cm length) for 10 minutes. During test, two mice of different genotypes were placed at opposite ends of the tube and allowed to walk to the middle. The match concluded when the one mouse (the dominant mouse) forced the other mouse (the submissive mouse) to retreat with all four paws outside of the tube (a "win" for the dominant mouse) (100-102). Each mouse underwent a total of three matches against three different opponents for counterbalancing. Videos were

recorded by Ethovision XT9 software as described above, and videos were manually scored by trained experimenters blind to genotype. The number of “wins” was reported as a percentage of total number of matches. Data were analyzed using an Exact Binomial Test with 0.5 as the probability of success (win or loss).

Resident-intruder aggression: Resident-intruder tests were used to assess aggression. Tests performed on consecutive days, where the resident mouse was exposed to an unfamiliar intruder mouse for 15 minutes (103, 104). A trial was terminated prematurely if blood was drawn, if an attack lasted continuously for 30 seconds, or if an intruder showed visible signs of injury after an attack. Resident mice were assessed for active aggression (darting, mounting, chasing/following, tail rattling, and boxing/parrying), as well as submissive behaviors (cowering, upright, running away). Intruder mice were assessed for passive defense (freezing, cowering, and digging). Behavior was recorded and videos scored manually by experimenters blind to genotype. Data were analyzed using a between groups analysis (one-way ANOVA) with genotype as the between-subjects factor.

Acknowledgements

We thank Dr. Ken Kwan, Mandy Lam, and Own Funk for their assistance with the Click-seq library preparation protocol and use of their microscope; Chris Gates for his assistance with RNA-seq analyses; and Clara Farrehi, Jordan Rich, and Demetri Tsirukis for their assistance with transcriptome analyses, global histone methylation Western blots, and brain histology, respectively. We also thank Drs. Sally Camper, Yali

Dou, Kenneth Kwan, Stephen Parker, Stephanie Bielas, Michael-Christopher Keogh, as well as the members of the Iwase and Bielas labs, for helpful discussions and critical review of the data.

Conflict of Interest

MW is CEO of Neurodigitech, LLC. The other authors declare that the research was conducted in the absence of any commercial or financial relationships that could be construed as a potential conflict of interest.

Author Contributions

CNV, NT, and SI conceived the study and designed the experiments. YAS performed global H3K4me3 analyses. RSP performed H3K4me3 ChIP-seq analyses. PMG analyzed RNA-seq data for activity-dependent genes. MW oversaw dendritic morphometry analyses. BR and KMC performed the mouse behavioral tests under the guidance of NT. CNV performed all other experiments and analyses. YD and KK provided key experimental recourse and made important intellectual contributions. All authors contributed to the writing and editing of the manuscript.

Funding

This work was funded by an NIH National Research Service Award T32-GM07544 (University of Michigan Predoctoral Genetics Training Program) from the National Institute of General Medicine Sciences (to CNV), an NIH National Research Service Award T32-HD079342 (University of Michigan Predoctoral Career Training in the

Reproductive Sciences Program) from the National Institute of Child Health and Human Development (NICHD) (to CNV), University of Michigan Rackham Predoctoral Research Grants (to CNV), a Michigan Institute for Clinical and Health Research fellowship (Translational Research Education Certificate, supported by UL1TR000433 and UL1TR002240) (to CNV), a University of Michigan Rackham Predoctoral Fellowship award (to CNV), an Autism Science Foundation Predoctoral Fellowship award (to CNV), an NIH NINDS Awards (R01NS089896 and R21NS104774) (to SI), Basil O'Connor Starter Scholar Research Awards from March of Dimes Foundation (to SI), and a Farrehi Family Foundation Grant (to SI).

Figure Legends

Figure 1. The H3K4 methylopathies and generation of the *Kmt2a-Kdm5c* double-mutant (DM) mouse. (A) Histone H3 lysine 4 (H3K4me) methyltransferases (writers) and demethylases (erasers) depicted by their ability to place or remove H3K4me. Reader proteins recognizing specific H3K4me substrates (arrows) are depicted below. Genes are listed next to their associated neurodevelopmental disorder. KMT2A and KDM5C are highlighted in purple and green, respectively. WDSTS: Weideman-Steiner Syndrome; ID: intellectual disability; ASD: autism spectrum disorder, CPRF: cleft palate, psychomotor retardation, and distinctive facial features; ARID: autosomal recessive ID; MRXSCJ: mental retardation, X-linked, syndromic, Claes-Jensen type. **(B)** Mouse breeding scheme crossing congenic 129S1/SvlmJ *Kmt2a*-heterozygous males with congenic C57/Bl6 *Kdm5c*-heterozygous females, resulting in F1 generation mice. Only males were used in this study. **(C)** Numbers of male offspring across 30 litters, showing Mendelian ratios of expected genotypes. **(D)** Left panel: Body weight of adult mice > 2 months of age (mean ± SEM, ****$p < 0.0001$ in One-way ANOVA). Right panel: Difference between group means of weight (mean ± 95% confidence intervals, *$p<0.05$, **$p<0.01$, ***$p<0.001$, ****$p<0.0001$ in Tukey multiple comparison test). **(E)** Body weight tracked from birth, postnatal day 1 (P1).

Figure 2. Altered H3K4me3 landscapes in the amygdala and rescue effect in DM. (A) H3K4me3 coverage in 2a-HET, 5c-KO, or DM compared to WT across the genome, that was partitioned into 1 kilobase (kb) bins. **(B-D)** *Kmt2a*-HET differentially-methylated

regions (DMRs), identified as peaks hypermethylated or hypomethylated compared to WT using MACS2 (81) (q < 0.1) **(B)**, their location at promoters, within genes (intragenic), or between genes (intergenic) **(C)**, and how many were rescued in DM **(D)**. **(E-G)** *Kdm5c*-KO DMRs, identified as peaks hypermethylated or depleted compared to WT **(E)**, their location at promoters, within genes (intragenic), or between genes (intergenic) **(F)**, and how many were rescued in DM **(G)**. **(H)** Overlap between all *Kdm5c*-KO and *Kmt2a*-HET DMRs. **(I)** Heatmap of H3K4me3 fold change relative to WT, of 996 shared DMRs between *Kmt2a*-HET and *Kdm5c*-KO. Scale indicates log2 fold change of depleted (blue) to enriched (yellow) H3K4me3. **(J-M)** Peak track view of two representative loci for each of the major genome areas: promoter **(J)**, intragenic **(K)**, and intergenic **(L)** DMRs rescued in DM, or un-rescued in DM **(M)**. **(N)** Heatmap of H3K4me3 fold change relative to WT, of 7,397 rescued DMRs. Side bars indicate patterns of rescued regions: solid bars = hypermethylated in 5c-KO, hypomethylated in 2a-HET; open bars = hypermethylated in both 5c-KO, and 2a-HET; dashed bars = hypermethylated in all 5c-KO, 2a-HET, and DM. Scale indicates log2 fold change of depleted (blue) to enriched (yellow) H3K4me3. We analyzed amygdala tissue from 2 to 3 animals for each genotype (see Methods).

Figure 3. Similar transcriptomes between the *Kdm5c*-KO and *Kmt2a*-HET and rescue effect in DM. (A) Transcriptome comparison across three mutant genotypes relative to WT, represented as log2 mean normalized counts from DESeq2 (91). Differentially-expressed (DE) genes were determined using a threshold of *p*-value < 0.01 as previously described (31). **(B)** Log2 fold change relative to WT, of expression of

all 466 DE genes identified (136 2a-HET + 127 5c-KO + 203 DM). Scale indicates log2 fold change of down- (blue) to up- (yellow) regulated expression. Histogram on scale indicates count of genes in each color category. **(C)** Overlap between DE genes across genotypes. **(D)** Intersection of DE genes from reciprocal categories in single mutants. **(C)** Volcano plots depicting rescue effect in DM on *Kdm5c*-KO and *Kmt2a*-HET DE genes. DM gene expression plotted in grey, as log2 fold change and *p*-value in DM compared to WT. Genes identified as DE in either single mutant shown as open circles. Any of these genes that fell within the $p > 0.1$ cutoff (red shaded box) were considered rescued in DM. Dashed line depicts $p = 0.01$ threshold for determining DE genes. **(F)** Log2 fold change relative to WT, of expression of all 118 rescued genes. Scale indicates log2 fold change of down- (blue) to up- (yellow) regulated expression. Histogram on scale indicates count of genes in each color category. We analyzed amygdala tissue from 3 animals for each genotype (see Methods).

Figure 4. Altered dendrite morphology of *Kdm5c*-KO and *Kmt2a*-HET was reversed in DM animals. (A) Representative images of basolateral amygdala (BLA) pyramidal neurons across all genotypes, depicting overall neuron morphology including dendrite lengths and dendritic spines. **(B and C)** Left panel: Total dendrite lengths **(B)** or spine density **(C)** (mean ± 95% *$p<0.05$, ****$p<0.0001$, One-way ANOVA). Right panel: Difference between group means (mean ± 95% confidence intervals, *$p<0.05$, **$p<0.01$, ***$p<0.001$, ****$p<0.0001$ in Tukey multiple comparison test). **(D)** Quantification of spine morphology subtypes, represented as percent of total spines counted. At least 20 neurons from 4 animals per genotype were quantified.

Figure 5. Deficit of memory-related behavior in *Kdm5c*-KO and its rescue in DM. **(A)** Contextual fear conditioning test. Left panel: Freezing levels after shock on test day (mean ± SEM, *$p < 0.05$ in One-way ANOVA). Right panel: Difference between group means of freezing (mean ± 95% confidence intervals, *$p<0.05$ in Least Significant Difference (LSD) test). **(B)** Novel object recognition test. Left panel: Preference for novel versus familiar object (mean ± SEM, *$p < 0.05$ in One-way ANOVA). Right panel: Difference between group means of freeze response (mean ± 95% confidence intervals, *$p<0.05$ in Least Significant Difference (LSD) test). **(C)** Response to mild foot-shock (mean ± 95% confidence intervals, no statistical significance [n.s.], One-way ANOVA). **(D)** Locomotor activity (mean ± 95% confidence intervals, no statistical significance [n.s.], One-way ANOVA). N=21 WT, N=16 2a-HET, N=16 5c-KO, and N=12 DM animals were used for all studies.

Figure 6. Differential impacts of double mutation in social behavior. (A) Three chamber test for social interaction. Left panel: preference for stranger versus toy mouse (mean ± SEM, **$p < 0.01$ in One-way ANOVA). Right panel: Difference between group means of preference (mean ± 95% confidence intervals, *$p<0.05$, **$p<0.01$ in Least Significant Difference (LSD) test). **(B)** Tube test for social dominance. Proportion of wins in matches of each mutant versus WT. Numbers on colored bars represent total number of wins for WT (grey, above) or each mutant (below) in every matchup. **$p<0.01$, ***$p<0.001$, Exact binomial test. **(C-L)** Resident intruder test. **(C)** Left panel: average number of all aggressive behaviors (mean ± SEM, *$p < 0.05$ in One-way ANOVA). Right

panel: Difference between group means of aggressive behaviors (mean ± 95% confidence intervals, *p<0.05 in Least Significant Difference (LSD) test). **(D-H)** Individual aggressive behaviors (mean ± SEM, **p < 0.01 in One-way ANOVA). N.s. depicts no statistical difference. **(I)** Left panel: average number of all submissive behaviors (mean ± SEM, *p < 0.05 in One-way ANOVA). Right panel: Difference between group means of submissive behaviors (mean ± 95% confidence intervals, **p<0.01, ***p<0.001 in Least Significant Difference (LSD) test). **(J-L)** Individual submissive behaviors (mean ± SEM, **p < 0.01 in One-way ANOVA). N.s. depicts no statistical difference. N=21 WT, N=16 2a-HET, N=16 5c-KO, and N=12 DM animals were used for all studies.

Supplementary Figure 1. Expression of KMT2A and KDM5C. (A) Expression of *Kmt2a* and *Kdm5c*, from FACS-sorted single cells of mouse visual cortex, shown in reads per kilobase of transcript per million mapped reads (RPKM). Neuronal cells: GABAergic (GABA), Glutamatergic (Glu). Non-neuronal cells: astrocytes (A); endothelial cells (E); microglia (M), oligodendrocyte precursor cells (OPC); oligodendrocytes (O); smooth muscle cells (SMC). Image credit: Broad Institute “Single Cell Portal” transcriptome of adult mouse visual cortex (38). **(B)** Expression of *Kmt2a* and *Kdm5c* mRNA from adult mouse brain, shown in log2 of raw expression value from *in situ* hybridization. Brain regions: Isocortex, olfactory areas (OLF), hippocampal formation (HPF), cortical subplate (CTXsp), striatum (STR), pallidum (PAL), thalamus (TH), hypothalamus (HY), midbrain (MB), pons (P), medulla (MY), cerebellum (CB). Image credit: Allen Institute, Allen Mouse Brain Atlas (2004) (34). **(C)** Expression of *KMT2A* and *KDM5C* transcripts, from developing and adult human brains, shown in RPKM.

Human development and adulthood were split into the following Periods: 1-7 fetal development; 8-9 birth and infancy; 10-11 childhood; 12 adolescence; and 13-15 adulthood. Image credit: Human Brain Transcriptome Atlas (36, 105)

Supplementary Figure 2. Genotype confirmation and gross brain morphology of mutant mice. (A-B) RNA-seq read coverage of *Kmt2a* **(A)** and *Kdm5c* **(B)** genes, and targeted exons (highlight). **(C)** Genotyping using genomic DNA, confirming presence of *Kmt2a* and/or *Kdm5c* deleted alleles ("del") only in appropriate genotypes. **(D)** Western blot for Kdm5c protein. Stars indicate non-specific bands present in all samples. GAPDH shown for equal loading. **(E)** Serial brain sections 30 μm thick stained with DAPI to mark nuclei. Sections shown at Bregma regions 1.41, 0.49, -2.15, and -2.91 mm (top to bottom). Regions highlighted: anterior forceps of the corpus callosum (fmi), caudate putamen (CPu), corpus callosum (cc), lateral ventricle (LV), piriform cortex (Pir), olfactory tubercle (Tu), hippocampal fields CA1 and CA2, dentate gyrus (DG), anteromedial nucleus (AM), third ventricle (3V), substantia nigra pars reticularis (SNR). Scale bar: 1mm.

Supplementary Figure 3. H3K4me3 in the amygdala. (A) Western blot of whole brain lysates showing unchanged global H3K4 methylation across genotypes. Total histone H3 was detected using an antibody recognizing the C-terminus of H3, and used as a control for equal loading. **(B)** Validation of H3K4me3 ChIP-seq specificity. Barcode reads originating from spike-in nucleosomes were counted. The two synthetic nucleosomes with the H3K4me3 barcodes dominated all ChIP samples, with

H3K4me1/2 nucleosomes rarely detected. **(C)** H3K4me3 coverage in 2a-HET, 5c-KO, or DM compared to WT at promoters (± 1 kb of transcription start sites). **(D)** Distribution of all H3K4me3 peaks across the genome, in all genotypes. **(E-F)** Log2 fold change of H3K4me3 coverage across genotypes relative to WT, at 2a-HET DMRs **(E)** or 5c-KO DMRs **(F)**. Scale indicates log2 fold change of depleted (blue) to enriched (yellow) H3K4me3. **(G-H)** H3K4me3 coverage of individual replicates at 2a-HET DMRs **(G)** or *Kdm5c*-KO DMRs **(H)** in all genotypes. Scale indicates low (light) to high (dark) H3K4me3 coverage. **(I-J)** Top five mammalian transcription factor motifs identified in 2a-HET **(I)** and 5c-KO **(J)** DMRs.

Supplementary Figure 4. Additional analyses of the RNA-seq dataset. (A) ERCC spike-in dose-response curves in each genotype, plotting expected vs. observed transcript counts. Each dot represents a spike-in RNA molecule. **(B)** Comparison of mean normalized counts of *Kdm5c*-KO from present study (grey dots) with our previous RNA-seq approach (31). Previously identified up- (yellow) and down- (blue) regulated genes show consistent patterns in the present study. **(C)** Intersection of up- and down-regulated DE genes across genotypes. **(D)** Fold change of DE genes across genotypes. Boxplot features depict: box, interquartile range (IQR); line, median; whiskers, proportion of IQR past low and high quartiles. **(E-F)** Volcano plots depicting similarity of gene expression patterns in *Kdm5c*-KO and *Kmt2a*-HET DE genes. Genes identified as DE in either single mutant shown as open circles. By and large, genes identified as up (yellow) or down (blue) in one category are expressed in the same direction in the reciprocal genotype. Dashed line depicts $p = 0.01$ threshold for determining DE genes.

Supplementary Figure 5. Expression of genes that are activity-dependent, cell-type specific, or developmentally regulated, in mutant amygdala. (A-B) Expression of activity-dependent genes, which we previously identified by nascent RNA sequencing using cortical neurons in response to bicuculine (3,785 genes) **(A)**, or TTX (2,416 genes) **(B)** (106). Spearman Rank-order correlation test for all comparisons showed no linear relationship between fold changes of either set of activity-dependent genes and DE genes in the mutant transcriptomes, indicating normal expression of activity-dependent genes in all three genotypes. **(C)** DE gene expression across cell types. Genes enriched in seven cell types: astrocytes (A), neurons (N), microglia/macrophages (M), oligodendrocyte precursor cells (Op), newly formed oligodendrocytes (On), myelinating oligodendrocytes (Om), endothelial cells (E). Data were obtained from Zhang et al. (93). None of the DE genes in the mutant amygdala show strong bias to a particular cell type. Boxplot features depict: box, interquartile range (IQR); line, median; whiskers, proportion of IQR past low and high quartiles. **(D-E)** We examined human adult male amygdala gene expression over time, from embryonic to adult ages. Preconception weeks (PCW), months (mo), years (yr). We examined trajectory of neurogeneisis (GO:0050769) or synaptic (GO:0007268) genes throughout normal development **(D)**. As expected, synaptic genes showed upward shift, while neurogenesis genes exhibited downward shift in their expression during the development. When we plotted the expression of our DE genes across genotypes throughout normal development, we did not find noticeable trends, except that DM down-regulated genes were more highly expressed compared to DE genes in other

genotypes **(E)**. Data credit: Allen Institute, BrainSpan Atlas of the Developing Human Brain (2010) (94).

Supplementary Figure 6. Integrative analysis of ChIP-seq and RNA-seq (A) Expression of genes associated with promoter- or intragenic-DMRs. **(B)** RNA-seq read depth and H3K4me3 ChIP-seq read depth at 5c-KO intergenic DMRs, across genotypes. **(C)** H3K4me3 coverage at promoter regions of differentially expressed (DE) genes. **(D)** H3K4me3 coverage at promoter regions of rescued genes. Boxplot features depict: box, interquartile range (IQR); line, median; notch, confidence interval for median; whiskers, proportion of IQR past low and high quartiles.

Supplementary Figure 7. Behaviors during resident-intruder test. Differences between group means all aggressive **(A-E)** and submissive **(F-H)** behaviors (mean ± 95% confidence intervals, *p<0.05, **p<0.01 in Least Significant Difference (LSD) test).

Supplementary Figure 8. Molecular alterations unique to DM mice. (A) Representative genome browser view of extended H3K4me3 boundary observed at some DM DMRs. **(B)** Volcano plots depicting larger gene misregulation effects in the DM transcriptome. Transcriptome of 2a-HET or 5c-KO plotted as grey dots. Genes identified as DE in DM shown as colored open circles. A majority of these genes fell below the line of significance in either single mutant, indicating DM leads to the misregulation of genes that were previously not DE in either 2a-HET or 5c-KO. Dashed line depicts p = 0.01 threshold for determining DE genes. **(C)** Fold change of DM DE

genes across genotypes. DM up- and down-regulated genes were expressed in the same direction in each single mutant, though DM leads to a more pronounced up- or down-regulation effect. Boxplot features depict: box, interquartile range (IQR); line, median; whiskers, proportion of IQR past low and high quartiles.

References

1. Faundes V, Newman WG, Bernardini L, Canham N, Clayton-Smith J, Dallapiccola B, et al. Histone Lysine Methylases and Demethylases in the Landscape of Human Developmental Disorders. *Am J Hum Genet.* 2018;102(1):175-87.
2. De Rubeis S, He X, Goldberg AP, Poultney CS, Samocha K, Ercument Cicek A, et al. Synaptic, transcriptional and chromatin genes disrupted in autism. *Nature.* 2014;515(7526):209-15.
3. Iossifov I, O'Roak BJ, Sanders SJ, Ronemus M, Krumm N, Levy D, et al. The contribution of de novo coding mutations to autism spectrum disorder. *Nature.* 2014;515(7526):216-21.
4. Kouzarides T. Chromatin modifications and their function. *Cell.* 2007;128(4):693-705.
5. Taverna SD, Li H, Ruthenburg AJ, Allis CD, and Patel DJ. How chromatin-binding modules interpret histone modifications: lessons from professional pocket pickers. *Nat Struct Mol Biol.* 2007;14(11):1025-40.
6. Allis CD, Berger SL, Cote J, Dent S, Jenuwien T, Kouzarides T, et al. New nomenclature for chromatin-modifying enzymes. *Cell.* 2007;131(4):633-6.
7. Iwase S, Berube NG, Zhou Z, Kasri NN, Battaglioli E, Scandaglia M, et al. Epigenetic Etiology of Intellectual Disability. *The Journal of neuroscience : the official journal of the Society for Neuroscience.* 2017;37(45):10773-82.
8. Ronan JL, Wu W, and Crabtree GR. From neural development to cognition: unexpected roles for chromatin. *Nat Rev Genet.* 2013;14(5):347-59.
9. Iwase S, and Shi Y. Histone and DNA modifications in mental retardation. *Progress in drug research Fortschritte der Arzneimittelforschung Progres des recherches pharmaceutiques.* 2011;67:147-73.
10. Barski A, Cuddapah S, Cui K, Roh TY, Schones DE, Wang Z, et al. High-resolution profiling of histone methylations in the human genome. *Cell.* 2007;129(4):823-37.
11. Heintzman ND, Stuart RK, Hon G, Fu Y, Ching CW, Hawkins RD, et al. Distinct and predictive chromatin signatures of transcriptional promoters and enhancers in the human genome. *Nat Genet.* 2007;39(3):311-8.
12. Vermeulen M, Mulder KW, Denissov S, Pijnappel WW, van Schaik FM, Varier RA, et al. Selective anchoring of TFIID to nucleosomes by trimethylation of histone H3 lysine 4. *Cell.* 2007;131(1):58-69.
13. Lauberth SM, Nakayama T, Wu X, Ferris AL, Tang Z, Hughes SH, et al. H3K4me3 Interactions with TAF3 Regulate Preinitiation Complex Assembly and Selective Gene Activation. *Cell.* 2013;152(5):1021-36.
14. Local A, Huang H, Albuquerque CP, Singh N, Lee AY, Wang W, et al. Identification of H3K4me1-associated proteins at mammalian enhancers. *Nat Genet.* 2018;50(1):73-82.
15. Cheung I, Shulha HP, Jiang Y, Matevossian A, Wang J, Weng Z, et al. Developmental regulation and individual differences of neuronal H3K4me3 epigenomes in the prefrontal cortex. *Proceedings of the National Academy of Sciences of the United States of America.* 2010;107(19):8824-9.

988 16. Shulha HP, Cheung I, Whittle C, Wang J, Virgil D, Lin CL, et al. Epigenetic signatures
989 of autism: trimethylated H3K4 landscapes in prefrontal neurons. *Arch Gen*
990 *Psychiatry.* 2012;69(3):314-24.
991 17. Shulha HP, Crisci JL, Reshetov D, Tushir JS, Cheung I, Bharadwaj R, et al. Human-
992 specific histone methylation signatures at transcription start sites in prefrontal
993 neurons. *PLoS biology.* 2012;10(11):e1001427.
994 18. Vallianatos CN, and Iwase S. Disrupted intricacy of histone H3K4 methylation in
995 neurodevelopmental disorders. *Epigenomics.* 2015;7(3):503-19.
996 19. Alarcon JM, Malleret G, Touzani K, Vronskaya S, Ishii S, Kandel ER, et al. Chromatin
997 acetylation, memory, and LTP are impaired in CBP+/- mice: a model for the
998 cognitive deficit in Rubinstein-Taybi syndrome and its amelioration. *Neuron.*
999 2004;42(6):947-59.
1000 20. Bjornsson HT, Benjamin JS, Zhang L, Weissman J, Gerber EE, Chen YC, et al. Histone
1001 deacetylase inhibition rescues structural and functional brain deficits in a mouse
1002 model of Kabuki syndrome. *Science translational medicine.* 2014;6(256):256ra135.
1003 21. Park J, Thomas S, and Munster PN. Epigenetic modulation with histone deacetylase
1004 inhibitors in combination with immunotherapy. *Epigenomics.* 2015;7(4):641-52.
1005 22. Strom SP, Lozano R, Lee H, Dorrani N, Mann J, O'Lague PF, et al. De Novo variants in
1006 the KMT2A (MLL) gene causing atypical Wiedemann-Steiner syndrome in two
1007 unrelated individuals identified by clinical exome sequencing. *BMC Med Genet.*
1008 2014;15:49.
1009 23. Jones WD, Dafou D, McEntagart M, Woollard WJ, Elmslie FV, Holder-Espinasse M, et
1010 al. De Novo Mutations in MLL Cause Wiedemann-Steiner Syndrome. *American*
1011 *Journal of Human Genetics.* 2012;91(2):358-64.
1012 24. Claes S, Devriendt K, Van Goethem G, Roelen L, Meireleire J, Raeymaekers P, et al.
1013 Novel syndromic form of X-linked complicated spastic paraplegia. *Am J Med Genet.*
1014 2000;94(1):1-4.
1015 25. Jensen LR, Amende M, Gurok U, Moser B, Gimmel V, Tzschach A, et al. Mutations in
1016 the JARID1C gene, which is involved in transcriptional regulation and chromatin
1017 remodeling, cause X-linked mental retardation. *Am J Hum Genet.* 2005;76(2):227-36.
1018 26. Adegbola A, Gao H, Sommer S, and Browning M. A novel mutation in JARID1C/SMCX
1019 in a patient with autism spectrum disorder (ASD). *American journal of medical*
1020 *genetics Part A.* 2008;146A(4):505-11.
1021 27. Vallianatos CN, Farrehi C, Friez MJ, Burmeister M, Keegan CE, and Iwase S. Altered
1022 Gene-Regulatory Function of KDM5C by a Novel Mutation Associated With Autism
1023 and Intellectual Disability. *Front Mol Neurosci.* 2018;11:104.
1024 28. Gupta S, Kim SY, Artis S, Molfese DL, Schumacher A, Sweatt JD, et al. Histone
1025 methylation regulates memory formation. *The Journal of neuroscience : the official*
1026 *journal of the Society for Neuroscience.* 2010;30(10):3589-99.
1027 29. Jakovcevski M, Ruan H, Shen EY, Dincer A, Javidfar B, Ma Q, et al. Neuronal
1028 Kmt2a/Mll1 histone methyltransferase is essential for prefrontal synaptic plasticity
1029 and working memory. *The Journal of neuroscience : the official journal of the Society*
1030 *for Neuroscience.* 2015;35(13):5097-108.
1031 30. Kerimoglu C, Sakib MS, Jain G, Benito E, Burkhardt S, Capece V, et al. KMT2A and
1032 KMT2B Mediate Memory Function by Affecting Distinct Genomic Regions. *Cell Rep.*
1033 2017;20(3):538-48.

1034 31. Iwase S, Brookes E, Agarwal S, Badeaux AI, Ito H, Vallianatos CN, et al. A Mouse
1035 Model of X-linked Intellectual Disability Associated with Impaired Removal of
1036 Histone Methylation. *Cell reports.* 2016.
1037 32. Scandaglia M, Lopez-Atalaya JP, Medrano-Fernandez A, Lopez-Cascales MT, Del
1038 Blanco B, Lipinski M, et al. Loss of Kdm5c Causes Spurious Transcription and
1039 Prevents the Fine-Tuning of Activity-Regulated Enhancers in Neurons. *Cell reports.*
1040 2017;21(1):47-59.
1041 33. Hawrylycz MJ, Lein ES, Guillozet-Bongaarts AL, Shen EH, Ng L, Miller JA, et al. An
1042 anatomically comprehensive atlas of the adult human brain transcriptome. *Nature.*
1043 2012;489(7416):391-9.
1044 34. Lein ES, Hawrylycz MJ, Ao N, Ayres M, Bensinger A, Bernard A, et al. Genome-wide
1045 atlas of gene expression in the adult mouse brain. *Nature.* 2007;445(7124):168-76.
1046 35. Zhang XQ, Wang ZL, Poon MW, and Yang JH. Spatial-temporal transcriptional
1047 dynamics of long non-coding RNAs in human brain. *Hum Mol Genet.*
1048 2017;26(16):3202-11.
1049 36. Pletikos M, Sousa AM, Sedmak G, Meyer KA, Zhu Y, Cheng F, et al. Temporal
1050 specification and bilaterality of human neocortical topographic gene expression.
1051 *Neuron.* 2014;81(2):321-32.
1052 37. Johnson MB, Kawasawa YI, Mason CE, Krsnik Z, Coppola G, Bogdanovic D, et al.
1053 Functional and evolutionary insights into human brain development through global
1054 transcriptome analysis. *Neuron.* 2009;62(4):494-509.
1055 38. Tasic B, Menon V, Nguyen TN, Kim TK, Jarsky T, Yao Z, et al. Adult mouse cortical cell
1056 taxonomy revealed by single cell transcriptomics. *Nature neuroscience.*
1057 2016;19(2):335-46.
1058 39. Cao F, Townsend EC, Karatas H, Xu J, Li L, Lee S, et al. Targeting MLL1 H3K4
1059 methyltransferase activity in mixed-lineage leukemia. *Mol Cell.* 2014;53(2):247-61.
1060 40. Dou YL, Milne TA, Ruthenburg AJ, Lee S, Lee JW, Verdine GL, et al. Regulation of
1061 MLL1 H3K4 methyltransferase activity by its core components. *Nature Structural &*
1062 *Molecular Biology.* 2006;13(8):713-9.
1063 41. Iwase S, Lan F, Bayliss P, de la Torre-Ubieta L, Huarte M, Qi HH, et al. The X-linked
1064 mental retardation gene SMCX/JARID1C defines a family of histone H3 lysine 4
1065 demethylases. *Cell.* 2007;128(6):1077-88.
1066 42. Tahiliani M, Mei PC, Fang R, Leonor T, Rutenberg M, Shimizu F, et al. The histone
1067 H3K4 demethylase SMCX links REST target genes to X-linked mental retardation.
1068 *Nature.* 2007;447(7144):601-+.
1069 43. Shah RN, Grzybowski AT, Cornett EM, Johnstone AL, Dickson BM, Boone BA, et al.
1070 Examining the Roles of H3K4 Methylation States with Systematically Characterized
1071 Antibodies. *Molecular cell.* 2018;72(1):162-77 e7.
1072 44. Jaworski E, and Routh A. ClickSeq: Replacing Fragmentation and Enzymatic Ligation
1073 with Click-Chemistry to Prevent Sequence Chimeras. *Methods Mol Biol.*
1074 2018;1712:71-85.
1075 45. Zhang H, Gayen S, Xiong J, Zhou B, Shanmugam AK, Sun Y, et al. MLL1 Inhibition
1076 Reprograms Epiblast Stem Cells to Naive Pluripotency. *Cell stem cell.*
1077 2016;18(4):481-94.
1078 46. Outchkourov NS, Muino JM, Kaufmann K, van Ijcken WF, Groot Koerkamp MJ, van
1079 Leenen D, et al. Balancing of histone H3K4 methylation states by the Kdm5c/SMCX

1080 histone demethylase modulates promoter and enhancer function. *Cell reports.*
1081 2013;3(4):1071-9.
1082 47. S G, E M, Y M-N, CN V, RS P, PM G, et al. biorxiv: Cold Spring Harbor Laboratory;
1083 2017.
1084 48. Nakamura K, Kodera H, Akita T, Shiina M, Kato M, Hoshino H, et al. De Novo
1085 mutations in GNAO1, encoding a Gαo subunit of heterotrimeric G proteins, cause
1086 epileptic encephalopathy. *Am J Hum Genet.* 2013;93(3):496-505.
1087 49. Kulkarni N, Tang S, Bhardwaj R, Bernes S, and Grebe TA. Progressive Movement
1088 Disorder in Brothers Carrying a GNAO1 Mutation Responsive to Deep Brain
1089 Stimulation. *J Child Neurol.* 2016;31(2):211-4.
1090 50. Lessel D, Gehbauer C, Bramswig NC, Schluth-Bolard C, Venkataramanappa S, van
1091 Gassen KLI, et al. BCL11B mutations in patients affected by a neurodevelopmental
1092 disorder with reduced type 2 innate lymphoid cells. *Brain.* 2018;141(8):2299-311.
1093 51. Webb EA, AlMutair A, Kelberman D, Bacchelli C, Chanudet E, Lescai F, et al. ARNT2
1094 mutation causes hypopituitarism, post-natal microcephaly, visual and renal
1095 anomalies. *Brain.* 2013;136(Pt 10):3096-105.
1096 52. Slavotinek AM, Stone EM, Mykytyn K, Heckenlively JR, Green JS, Heon E, et al.
1097 Mutations in MKKS cause Bardet-Biedl syndrome. *Nat Genet.* 2000;26(1):15-6.
1098 53. Katsanis N, Beales PL, Woods MO, Lewis RA, Green JS, Parfrey PS, et al. Mutations in
1099 MKKS cause obesity, retinal dystrophy and renal malformations associated with
1100 Bardet-Biedl syndrome. *Nat Genet.* 2000;26(1):67-70.
1101 54. Schaefer E, Durand M, Stoetzel C, Doray B, Viville B, Hellé S, et al. Molecular
1102 diagnosis reveals genetic heterogeneity for the overlapping MKKS and BBS
1103 phenotypes. *Eur J Med Genet.* 2011;54(2):157-60.
1104 55. Stone DL, Slavotinek A, Bouffard GG, Banerjee-Basu S, Baxevanis AD, Barr M, et al.
1105 Mutation of a gene encoding a putative chaperonin causes McKusick-Kaufman
1106 syndrome. *Nat Genet.* 2000;25(1):79-82.
1107 56. Tsurusaki Y, Okamoto N, Ohashi H, Kosho T, Imai Y, Hibi-Ko Y, et al. Mutations
1108 affecting components of the SWI/SNF complex cause Coffin-Siris syndrome. *Nat*
1109 *Genet.* 2012;44(4):376-8.
1110 57. Guissart C, Latypova X, Rollier P, Khan TN, Stamberger H, McWalter K, et al. Dual
1111 Molecular Effects of Dominant RORA Mutations Cause Two Variants of Syndromic
1112 Intellectual Disability with Either Autism or Cerebellar Ataxia. *Am J Hum Genet.*
1113 2018;102(5):744-59.
1114 58. Miyazaki T, Hashimoto K, Uda A, Sakagami H, Nakamura Y, Saito SY, et al.
1115 Disturbance of cerebellar synaptic maturation in mutant mice lacking BSRPs, a novel
1116 brain-specific receptor-like protein family. *FEBS Lett.* 2006;580(17):4057-64.
1117 59. Penzes P, Cahill ME, Jones KA, VanLeeuwen JE, and Woolfrey KM. Dendritic spine
1118 pathology in neuropsychiatric disorders. *Nat Neurosci.* 2011;14(3):285-93.
1119 60. Dierssen M, and Ramakers GJ. Dendritic pathology in mental retardation: from
1120 molecular genetics to neurobiology. *Genes Brain Behav.* 2006;5 Suppl 2:48-60.
1121 61. Xu X, Miller EC, and Pozzo-Miller L. Dendritic spine dysgenesis in Rett syndrome.
1122 *Front Neuroanat.* 2014;8:97.
1123 62. Irwin SA, Galvez R, and Greenough WT. Dendritic spine structural anomalies in
1124 fragile-X mental retardation syndrome. *Cereb Cortex.* 2000;10(10):1038-44.

1125 63. Arikkath J. Molecular mechanisms of dendrite morphogenesis. *Front Cell Neurosci.*
1126 2012;6:61.
1127 64. Maren S. Neurobiology of Pavlovian fear conditioning. *Annual review of neuroscience.*
1128 2001;24:897-931.
1129 65. Wang F, Kessels HW, and Hu H. The mouse that roared: neural mechanisms of social
1130 hierarchy. *Trends Neurosci.* 2014;37(11):674-82.
1131 66. Kim B, Colon E, Chawla S, Vandenberg LN, and Suvorov A. Endocrine disruptors alter
1132 social behaviors and indirectly influence social hierarchies via changes in body
1133 weight. *Environ Health.* 2015;14:64.
1134 67. Varholick JA, Bailoo JD, Palme R, and Würbel H. Phenotypic variability between
1135 Social Dominance Ranks in laboratory mice. *Sci Rep.* 2018;8(1):6593.
1136 68. Eissenberg JC, and Shilatifard A. Histone H3 lysine 4 (H3K4) methylation in
1137 development and differentiation. *Dev Biol.* 2010;339(2):240-9.
1138 69. Shilatifard A. The COMPASS family of histone H3K4 methylases: mechanisms of
1139 regulation in development and disease pathogenesis. *Annual review of biochemistry.*
1140 2012;81:65-95.
1141 70. Mishra S, Van Rechem C, Pal S, Clarke TL, Chakraborty D, Mahan SD, et al. Cross-talk
1142 between Lysine-Modifying Enzymes Controls Site-Specific DNA Amplifications. *Cell.*
1143 2018;175(6):1716.
1144 71. Cao K, Collings CK, Morgan MA, Marshall SA, Rendleman EJ, Ozark PA, et al. An
1145 Mll4/COMPASS-Lsd1 epigenetic axis governs enhancer function and pluripotency
1146 transition in embryonic stem cells. *Sci Adv.* 2018;4(1):eaap8747.
1147 72. Wiedemann HR. Genital overgrowth in the EMG syndrome. *Am J Med Genet.*
1148 1989;32(2):255-6.
1149 73. Felix-Ortiz AC, and Tye KM. Amygdala inputs to the ventral hippocampus
1150 bidirectionally modulate social behavior. *J Neurosci.* 2014;34(2):586-95.
1151 74. McCann KE, Sinkiewicz DM, Rosenhauer AM, Beach LQ, and Huhman KL.
1152 Transcriptomic Analysis Reveals Sex-Dependent Expression Patterns in the
1153 Basolateral Amygdala of Dominant and Subordinate Animals After Acute Social
1154 Conflict. *Mol Neurobiol.* 2018.
1155 75. Levinson DM, Reeves DL, and Buchanan DR. Reductions in aggression and
1156 dominance status in guinea pigs following bilateral lesions in the basolateral
1157 amygdala or lateral septum. *Physiol Behav.* 1980;25(6):963-71.
1158 76. McGregor A, and Herbert J. Differential effects of excitotoxic basolateral and
1159 corticomedial lesions of the amygdala on the behavioural and endocrine responses
1160 to either sexual or aggression-promoting stimuli in the male rat. *Brain Res.*
1161 1992;574(1-2):9-20.
1162 77. Felix-Ortiz AC, Burgos-Robles A, Bhagat ND, Leppla CA, and Tye KM. Bidirectional
1163 modulation of anxiety-related and social behaviors by amygdala projections to the
1164 medial prefrontal cortex. *Neuroscience.* 2016;321:197-209.
1165 78. McMahon KA, Hiew SY, Hadjur S, Veiga-Fernandes H, Menzel U, Price AJ, et al. Mll
1166 has a critical role in fetal and adult hematopoietic stem cell self-renewal. *Cell stem*
1167 *cell.* 2007;1(3):338-45.
1168 79. Brind'Amour J, Liu S, Hudson M, Chen C, Karimi MM, and Lorincz MC. An ultra-low-
1169 input native ChIP-seq protocol for genome-wide profiling of rare cell populations.
1170 *Nat Commun.* 2015;6:6033.

1171 80. Grzybowski AT, Chen Z, and Ruthenburg AJ. Calibrating ChIP-Seq with Nucleosomal
1172 Internal Standards to Measure Histone Modification Density Genome Wide. *Mol Cell.*
1173 2015;58(5):886-99.
1174 81. Zhang Y, Liu T, Meyer CA, Eeckhoute J, Johnson DS, Bernstein BE, et al. Model-based
1175 analysis of ChIP-Seq (MACS). *Genome biology.* 2008;9(9):R137.
1176 82. Heinz S, Benner C, Spann N, Bertolino E, Lin YC, Laslo P, et al. Simple combinations
1177 of lineage-determining transcription factors prime cis-regulatory elements required
1178 for macrophage and B cell identities. *Molecular cell.* 2010;38(4):576-89.
1179 83. Mudunuri U, Che A, Yi M, and Stephens RM. bioDBnet: the biological database
1180 network. *Bioinformatics.* 2009;25(4):555-6.
1181 84. Edgar R, Domrachev M, and Lash AE. Gene Expression Omnibus: NCBI gene
1182 expression and hybridization array data repository. *Nucleic Acids Res.*
1183 2002;30(1):207-10.
1184 85. Dobin A, Davis CA, Schlesinger F, Drenkow J, Zaleski C, Jha S, et al. STAR: ultrafast
1185 universal RNA-seq aligner. *Bioinformatics.* 2013;29(1):15-21.
1186 86. Smith T, Heger A, and Sudbery I. UMI-tools: modeling sequencing errors in Unique
1187 Molecular Identifiers to improve quantification accuracy. *Genome Res.*
1188 2017;27(3):491-9.
1189 87. Liao Y, Smyth GK, and Shi W. featureCounts: an efficient general purpose program
1190 for assigning sequence reads to genomic features. *Bioinformatics.* 2014;30(7):923-
1191 30.
1192 88. Ramírez F, Dündar F, Diehl S, Grüning BA, and Manke T. deepTools: a flexible
1193 platform for exploring deep-sequencing data. *Nucleic Acids Res.* 2014;42(Web Server
1194 issue):W187-91.
1195 89. Ramírez F, Ryan DP, Grüning B, Bhardwaj V, Kilpert F, Richter AS, et al. deepTools2:
1196 a next generation web server for deep-sequencing data analysis. *Nucleic Acids Res.*
1197 2016;44(W1):W160-5.
1198 90. Anders S, and Huber W. Differential expression analysis for sequence count data.
1199 *Genome biology.* 2010;11(10):R106.
1200 91. Love MI, Huber W, and Anders S. Moderated estimation of fold change and
1201 dispersion for RNA-seq data with DESeq2. *Genome Biol.* 2014;15(12):550.
1202 92. Khomtchouk BB, Hennessy JR, and Wahlestedt C. shinyheatmap: Ultra fast low
1203 memory heatmap web interface for big data genomics. *PLoS One.*
1204 2017;12(5):e0176334.
1205 93. Zhang Y, Chen K, Sloan SA, Bennett ML, Scholze AR, O'Keeffe S, et al. An RNA-
1206 sequencing transcriptome and splicing database of glia, neurons, and vascular cells
1207 of the cerebral cortex. *J Neurosci.* 2014;34(36):11929-47.
1208 94. Miller JA, Ding SL, Sunkin SM, Smith KA, Ng L, Szafer A, et al. Transcriptional
1209 landscape of the prenatal human brain. *Nature.* 2014;508(7495):199-206.
1210 95. Shmelkov SV, Hormigo A, Jing D, Proenca CC, Bath KG, Milde T, et al. Slitrk5
1211 deficiency impairs corticostriatal circuitry and leads to obsessive-compulsive-like
1212 behaviors in mice. *Nature medicine.* 2010;16(5):598-602, 1p following
1213 96. Vogel-Ciernia A, and Wood MA. Examining object location and object recognition
1214 memory in mice. *Curr Protoc Neurosci.* 2014;69:8.31.1-17.
1215 97. Tchessalova D, and Tronson NC. Memory deficits in males and females long after
1216 subchronic immune challenge. *Neurobiol Learn Mem.* 2019.

98. Keiser AA, Turnbull LM, Darian MA, Feldman DE, Song I, and Tronson NC. Sex Differences in Context Fear Generalization and Recruitment of Hippocampus and Amygdala during Retrieval. *Neuropsychopharmacology.* 2017;42(2):397-407.
99. Crawley JN. Mouse behavioral assays relevant to the symptoms of autism. *Brain Pathol.* 2007;17(4):448-59.
100. Zhou T, Zhu H, Fan Z, Wang F, Chen Y, Liang H, et al. History of winning remodels thalamo-PFC circuit to reinforce social dominance. *Science.* 2017;357(6347):162-8.
101. Larrieu T, Cherix A, Duque A, Rodrigues J, Lei H, Gruetter R, et al. Hierarchical Status Predicts Behavioral Vulnerability and Nucleus Accumbens Metabolic Profile Following Chronic Social Defeat Stress. *Curr Biol.* 2017;27(14):2202-10.e4.
102. Moretti P, Bouwknecht JA, Teague R, Paylor R, and Zoghbi HY. Abnormalities of social interactions and home-cage behavior in a mouse model of Rett syndrome. *Hum Mol Genet.* 2005;14(2):205-20.
103. Guzmán YF, Tronson NC, Jovasevic V, Sato K, Guedea AL, Mizukami H, et al. Fear-enhancing effects of septal oxytocin receptors. *Nat Neurosci.* 2013;16(9):1185-7.
104. Miczek KA, Maxson SC, Fish EW, and Faccidomo S. Aggressive behavioral phenotypes in mice. *Behav Brain Res.* 2001;125(1-2):167-81.
105. Kang HJ, Kawasawa YI, Cheng F, Zhu Y, Xu X, Li M, et al. Spatio-temporal transcriptome of the human brain. *Nature.* 2011;478(7370):483-9.
106. Garay P, Chen A, Tsukahara T, Kohen R, Althaus C, Wallner M, et al.: Biorxiv; 2019.

A

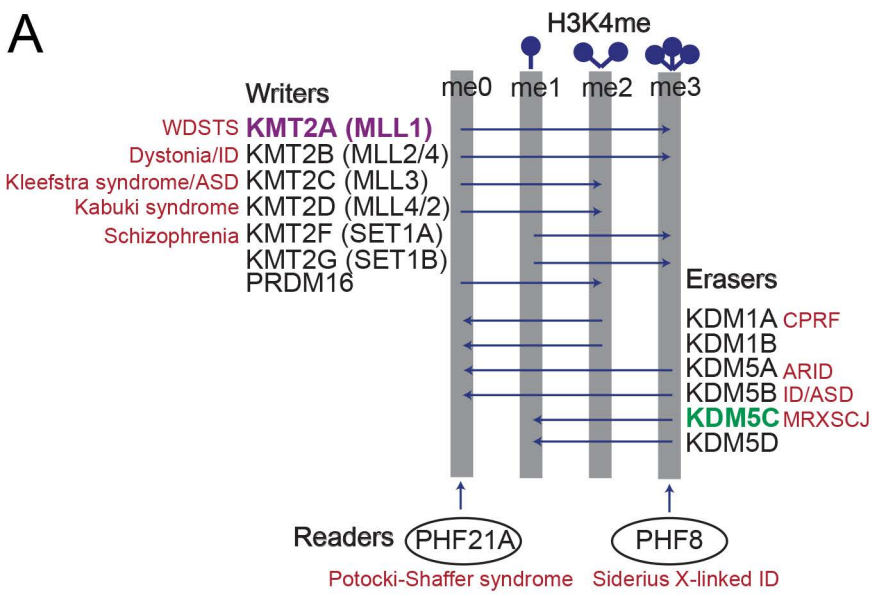

B

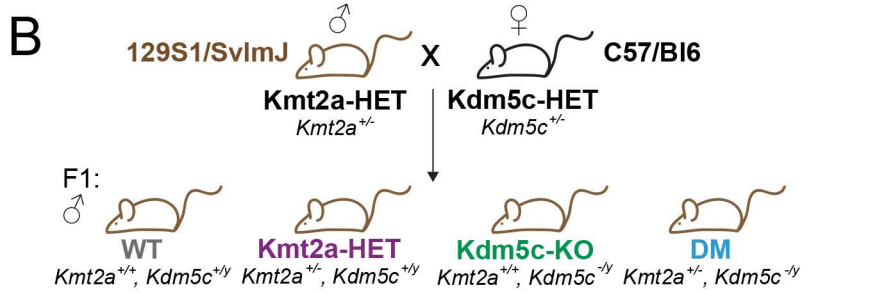

C

Number of offspring across 30 litters (% total males)			
WT	2a-HET	5c-KO	DM
17 (25%)	16 (23%)	21 (31%)	14 (21%)

D

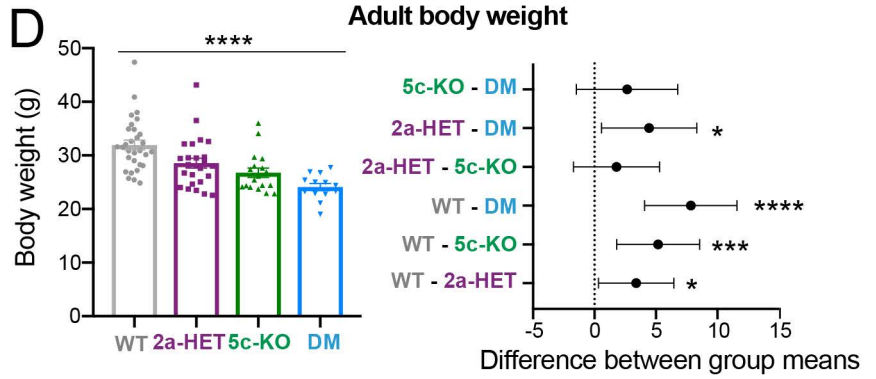

E

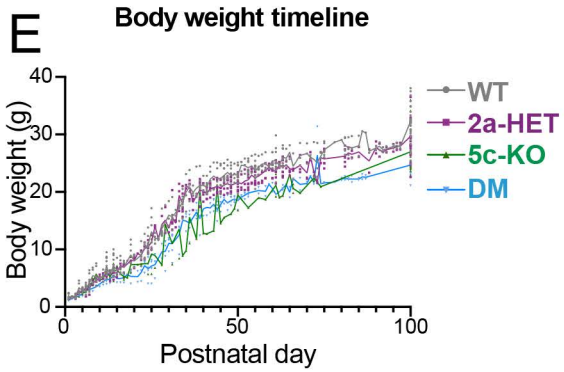

Figure 1

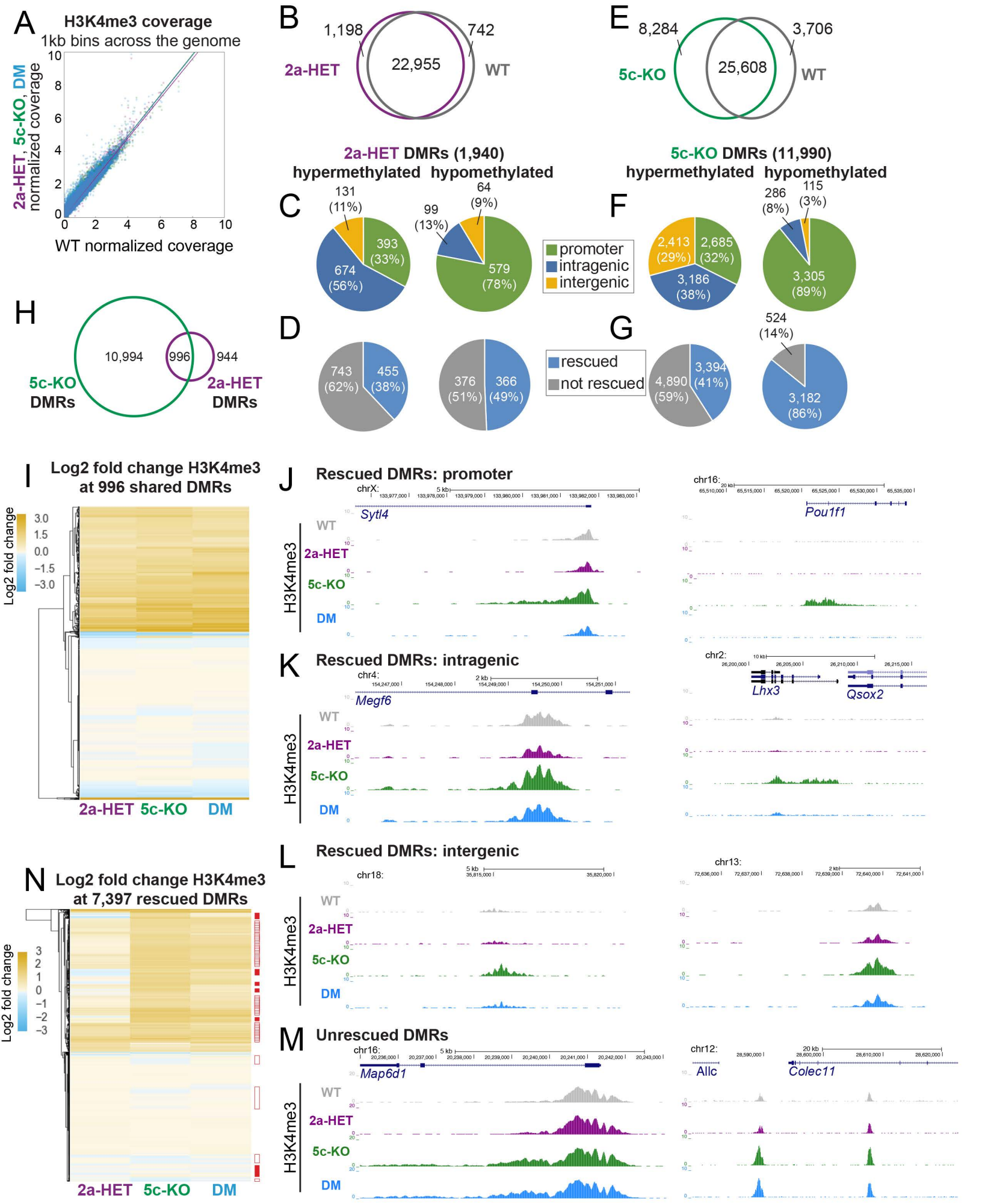
A
H3K4me3 coverage
1kb bins across the genome
2a-HET, 5c-KO, DM normalized coverage
WT normalized coverage
B
1,198
22,955
742
2a-HET
WT
E
8,284
25,608
3,706
5c-KO
WT
2a-HET DMRs (1,940)
hypermethylated
hypomethylated
5c-KO DMRs (11,990)
hypermethylated
hypomethylated
C
131 (11%)
393 (33%)
674 (56%)
99 (13%)
64 (9%)
579 (78%)
promoter
intragenic
intergenic
F
2,413 (29%)
2,685 (32%)
3,186 (38%)
286 (8%)
115 (3%)
3,305 (89%)
D
743 (62%)
455 (38%)
376 (51%)
366 (49%)
rescued
not rescued
G
4,890 (59%)
3,394 (41%)
524 (14%)
3,182 (86%)
H
10,994
996
944
5c-KO DMRs
2a-HET DMRs
I
Log2 fold change H3K4me3 at 996 shared DMRs
Log2 fold change
3.0
1.5
0.0
−1.5
−3.0
2a-HET
5c-KO
DM
J
Rescued DMRs: promoter
chrX:
Sytl4
chr16:
Pou1f1
H3K4me3
WT
2a-HET
5c-KO
DM
K
Rescued DMRs: intragenic
chr4:
Megf6
chr2:
Lhx3
Qsox2
L
Rescued DMRs: intergenic
chr18:
chr13:
M
Unrescued DMRs
chr16:
Map6d1
chr12:
Allc
Colec11
N
Log2 fold change H3K4me3 at 7,397 rescued DMRs
Log2 fold change
3
2
1
0
−1
−2
−3
2a-HET
5c-KO
DM

Figure 2

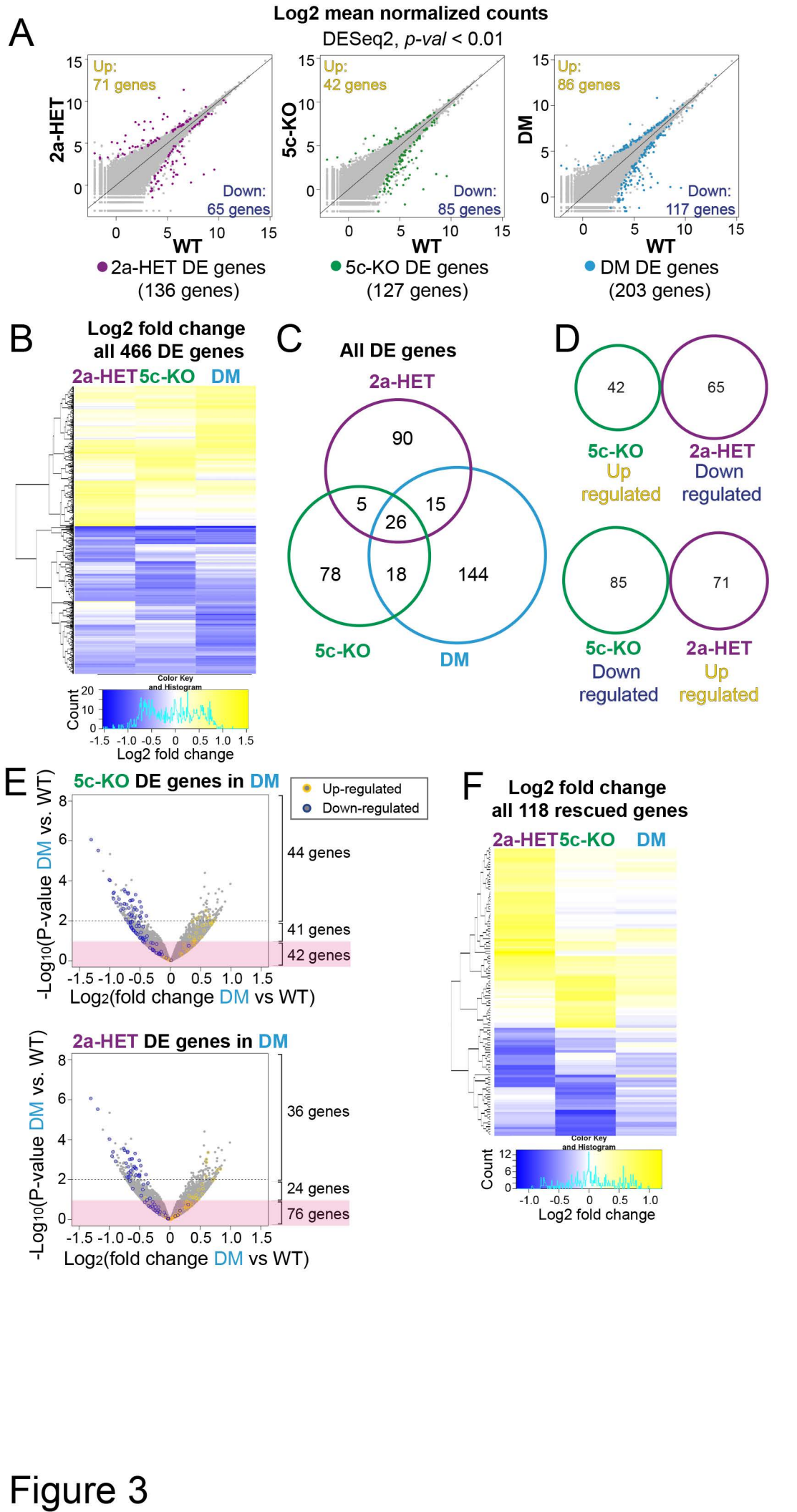
A
Log2 mean normalized counts
DESeq2, p-val < 0.01
Up: 71 genes
Down: 65 genes
2a-HET
WT
Up: 42 genes
Down: 85 genes
5c-KO
WT
Up: 86 genes
Down: 117 genes
DM
WT
2a-HET DE genes (136 genes)
5c-KO DE genes (127 genes)
DM DE genes (203 genes)
B
Log2 fold change all 466 DE genes
2a-HET 5c-KO DM
Color Key and Histogram
Count
Log2 fold change
C
All DE genes
2a-HET
90
5
15
26
78
18
144
5c-KO
DM
D
42
65
5c-KO Up regulated
2a-HET Down regulated
85
71
5c-KO Down regulated
2a-HET Up regulated
E
5c-KO DE genes in DM
Up-regulated
Down-regulated
44 genes
41 genes
42 genes
-Log10(P-value DM vs. WT)
Log2(fold change DM vs WT)
2a-HET DE genes in DM
36 genes
24 genes
76 genes
-Log10(P-value DM vs. WT)
Log2(fold change DM vs WT)
F
Log2 fold change all 118 rescued genes
2a-HET 5c-KO DM
Color Key and Histogram
Count
Log2 fold change

Figure 3

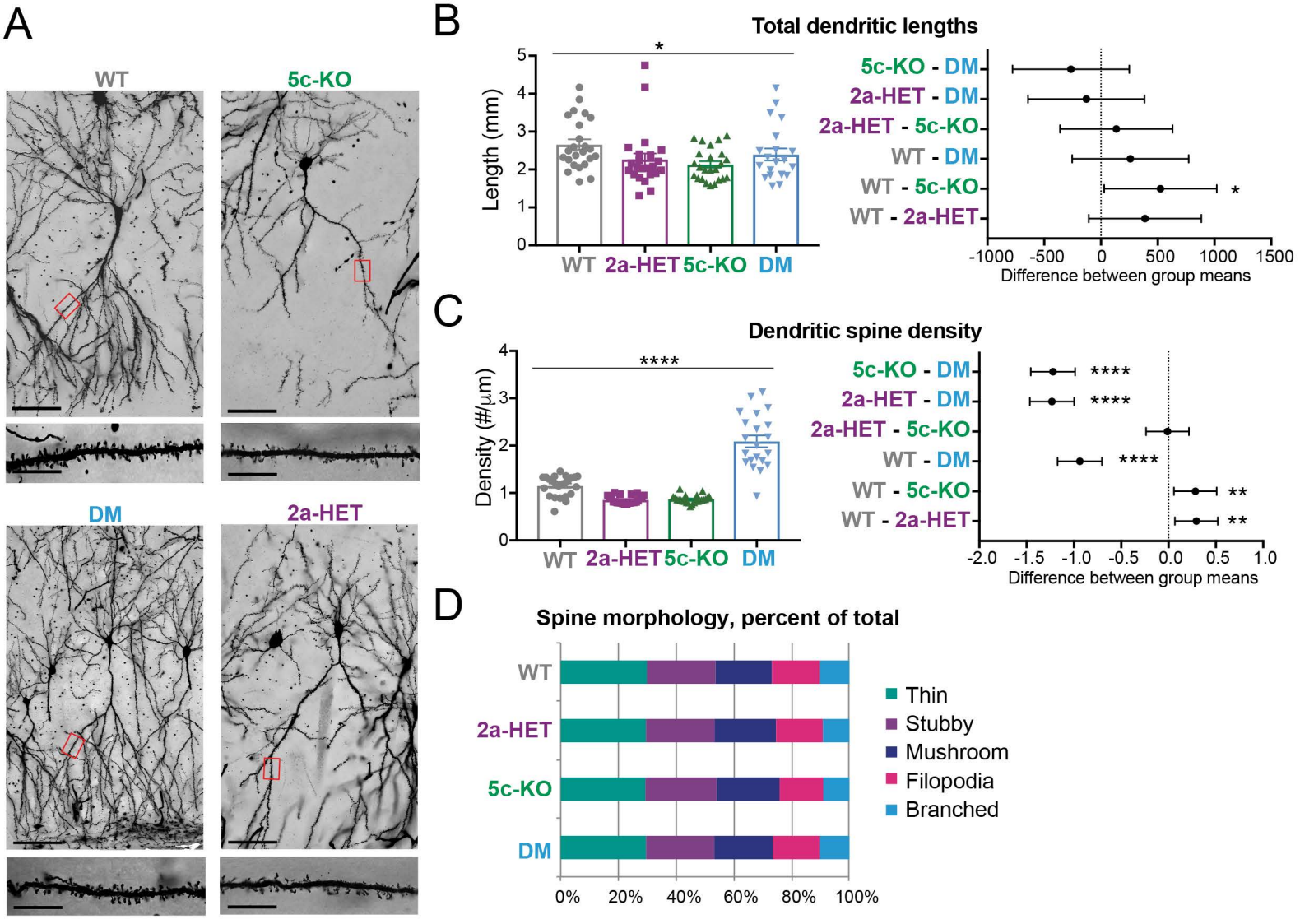
A
WT
5c-KO
DM
2a-HET
B
Total dendritic lengths
Length (mm)
*
WT
2a-HET
5c-KO
DM
5c-KO - DM
2a-HET - DM
2a-HET - 5c-KO
WT - DM
WT - 5c-KO
WT - 2a-HET
*
-1000
-500
0
500
1000
1500
Difference between group means
C
Dendritic spine density
Density (#/µm)
****
WT
2a-HET
5c-KO
DM
5c-KO - DM
2a-HET - DM
2a-HET - 5c-KO
WT - DM
WT - 5c-KO
WT - 2a-HET
****
****
****
**
**
-2.0
-1.5
-1.0
-0.5
0.0
0.5
1.0
Difference between group means
D
Spine morphology, percent of total
WT
2a-HET
5c-KO
DM
0%
20%
40%
60%
80%
100%
Thin
Stubby
Mushroom
Filopodia
Branched

Figure 4

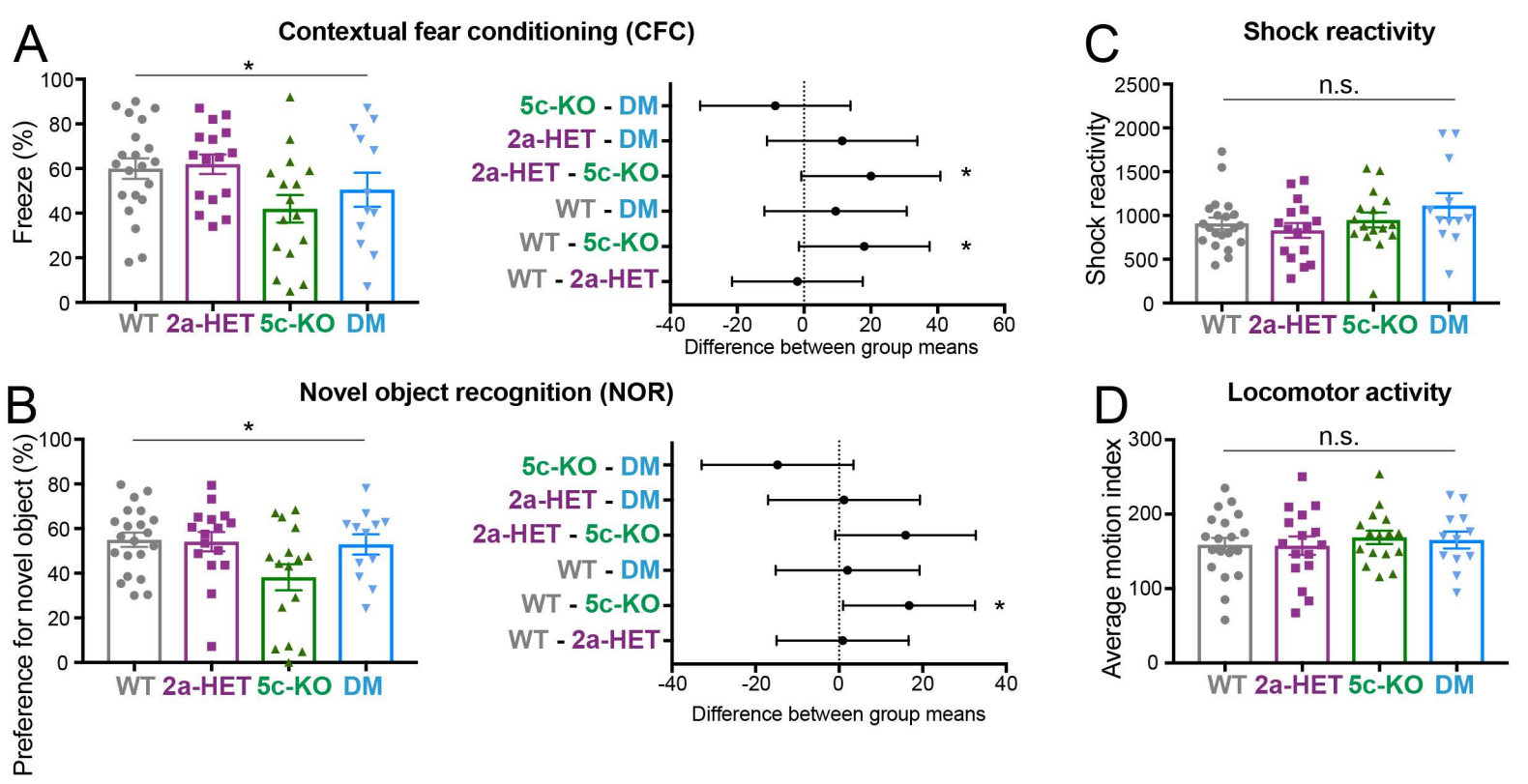
A
Contextual fear conditioning (CFC)
Freeze (%)
100
80
60
40
20
0
*
WT 2a-HET 5c-KO DM
5c-KO - DM
2a-HET - DM
2a-HET - 5c-KO
WT - DM
WT - 5c-KO
WT - 2a-HET
*
*
-40 -20 0 20 40 60
Difference between group means
C
Shock reactivity
Shock reactivity
2500
2000
1500
1000
500
0
n.s.
WT 2a-HET 5c-KO DM
B
Novel object recognition (NOR)
Preference for novel object (%)
100
80
60
40
20
0
*
WT 2a-HET 5c-KO DM
5c-KO - DM
2a-HET - DM
2a-HET - 5c-KO
WT - DM
WT - 5c-KO
WT - 2a-HET
*
-40 -20 0 20 40
Difference between group means
D
Locomotor activity
Average motion index
300
200
100
0
n.s.
WT 2a-HET 5c-KO DM

Figure 5

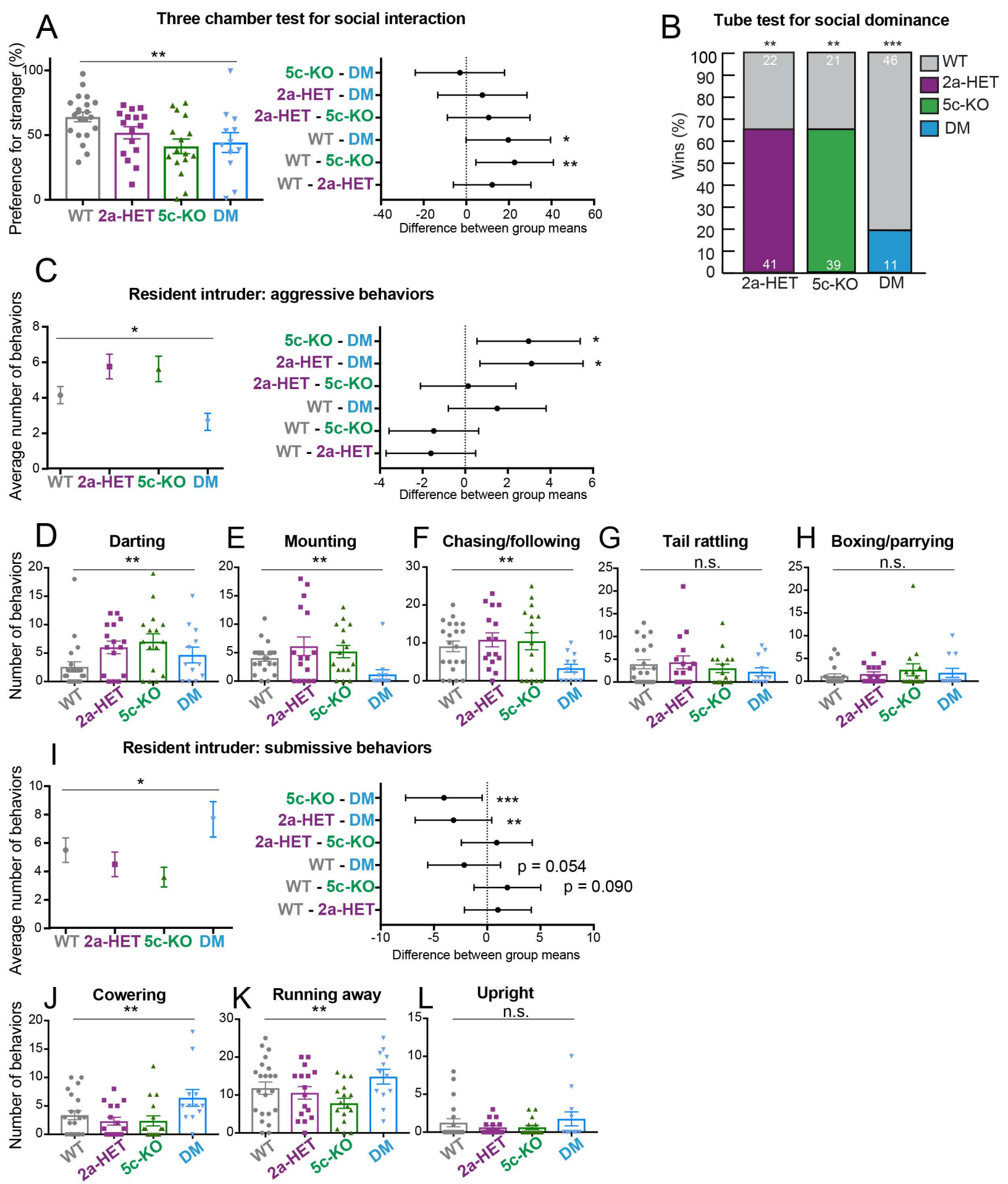
A
Three chamber test for social interaction
Preference for stranger (%)
WT 2a-HET 5c-KO DM
5c-KO - DM
2a-HET - DM
2a-HET - 5c-KO
WT - DM
WT - 5c-KO
WT - 2a-HET
Difference between group means
B
Tube test for social dominance
Wins (%)
2a-HET 5c-KO DM
WT
2a-HET
5c-KO
DM
C
Resident intruder: aggressive behaviors
Average number of behaviors
D
Darting
E
Mounting
F
Chasing/following
G
Tail rattling
H
Boxing/parrying
n.s.
Number of behaviors
I
Resident intruder: submissive behaviors
p = 0.054
p = 0.090
J
Cowering
K
Running away
L
Upright

Figure 6

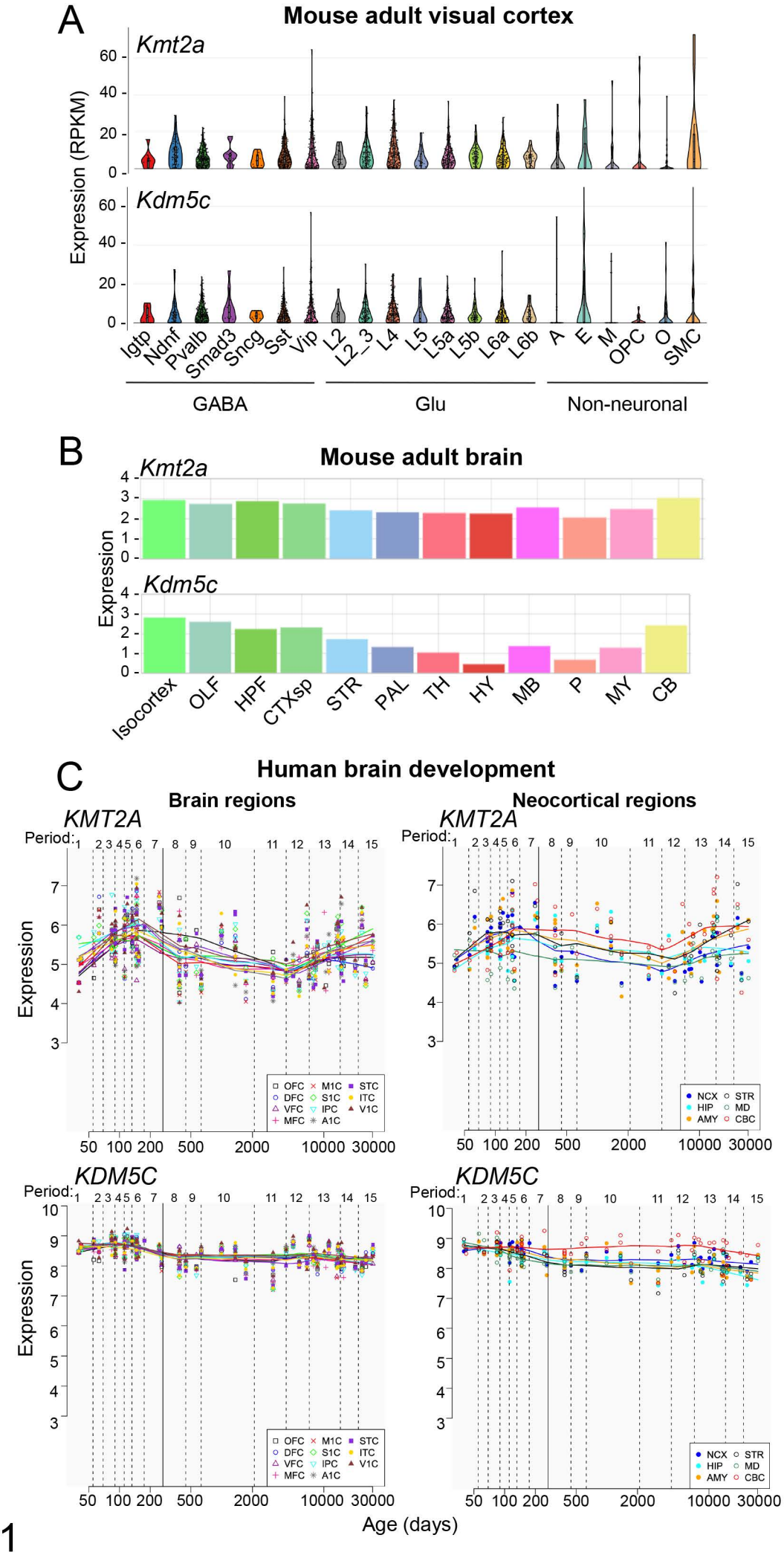

Supplementary Figure 1

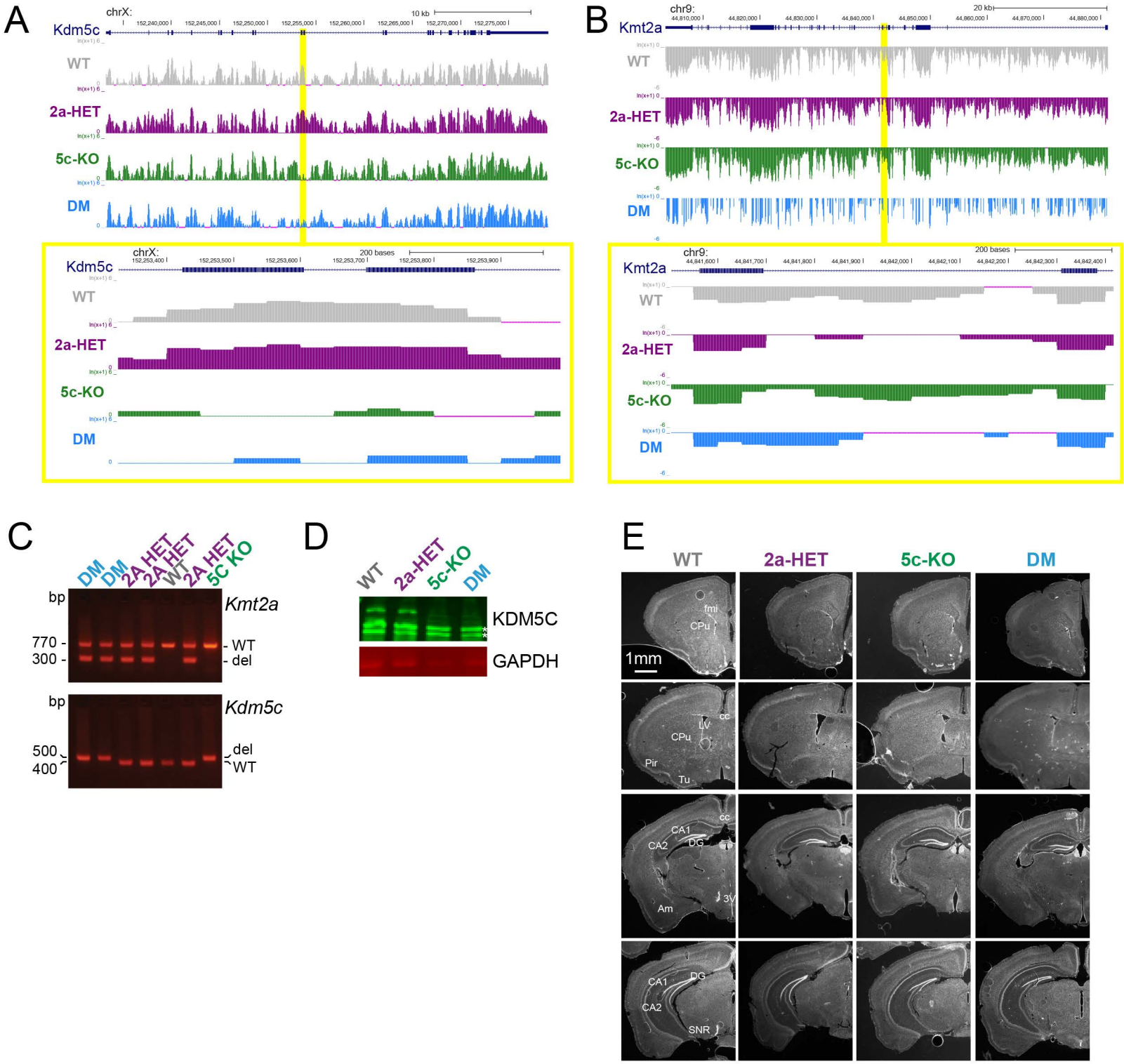

Supplementary Figure 2

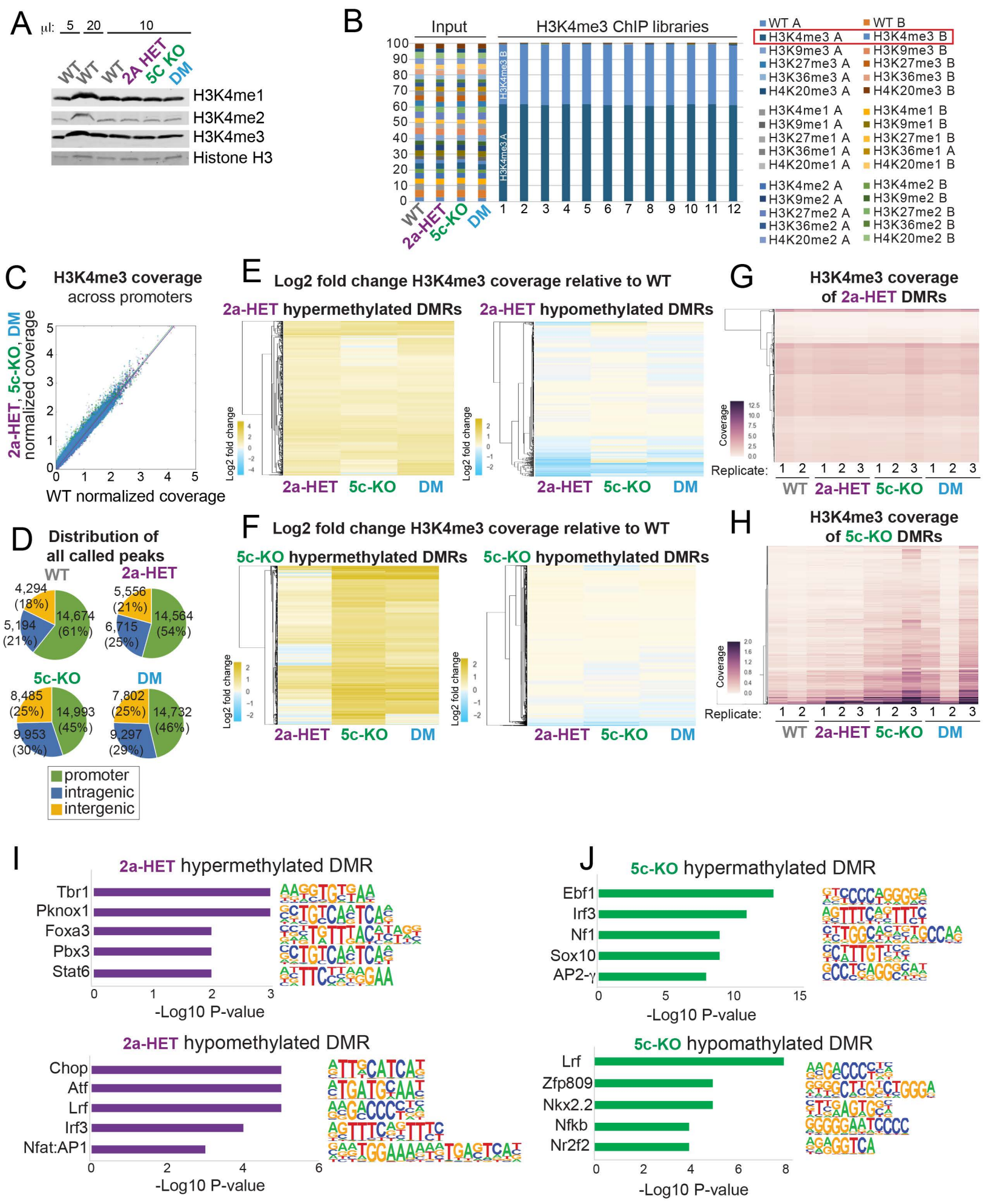

Supplementary Figure 3

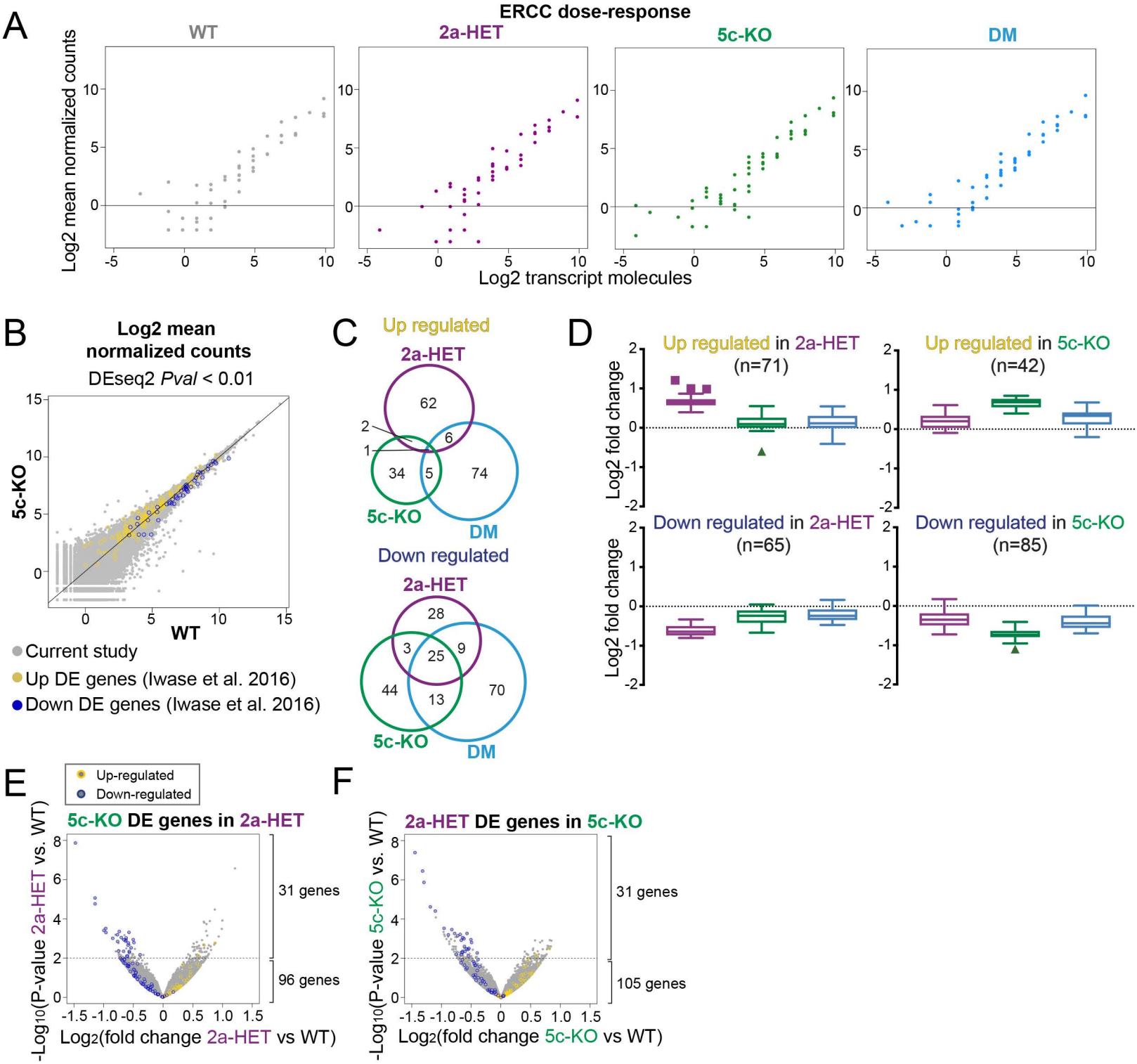

Supplementary Figure 4

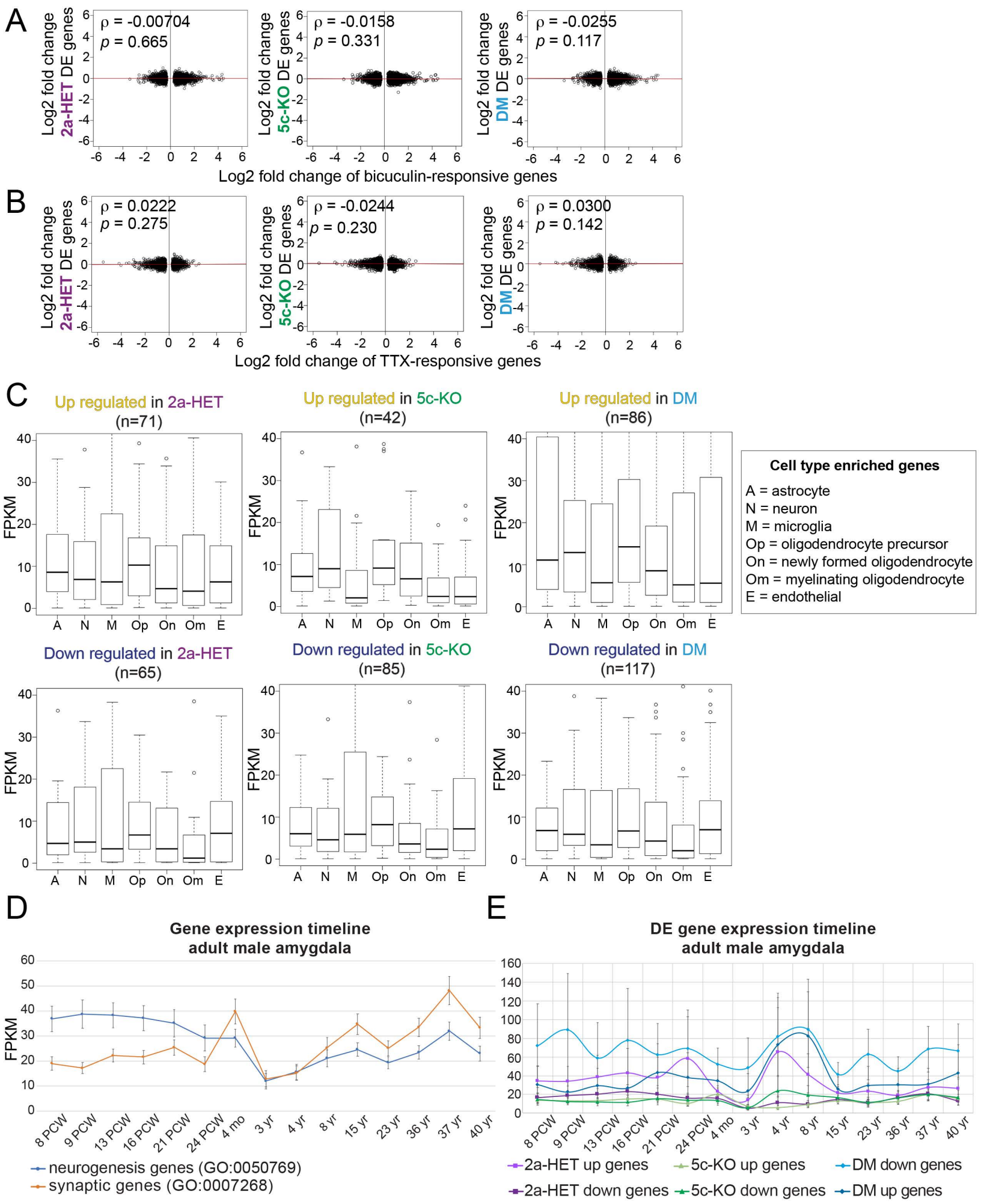

Supplementary Figure 5

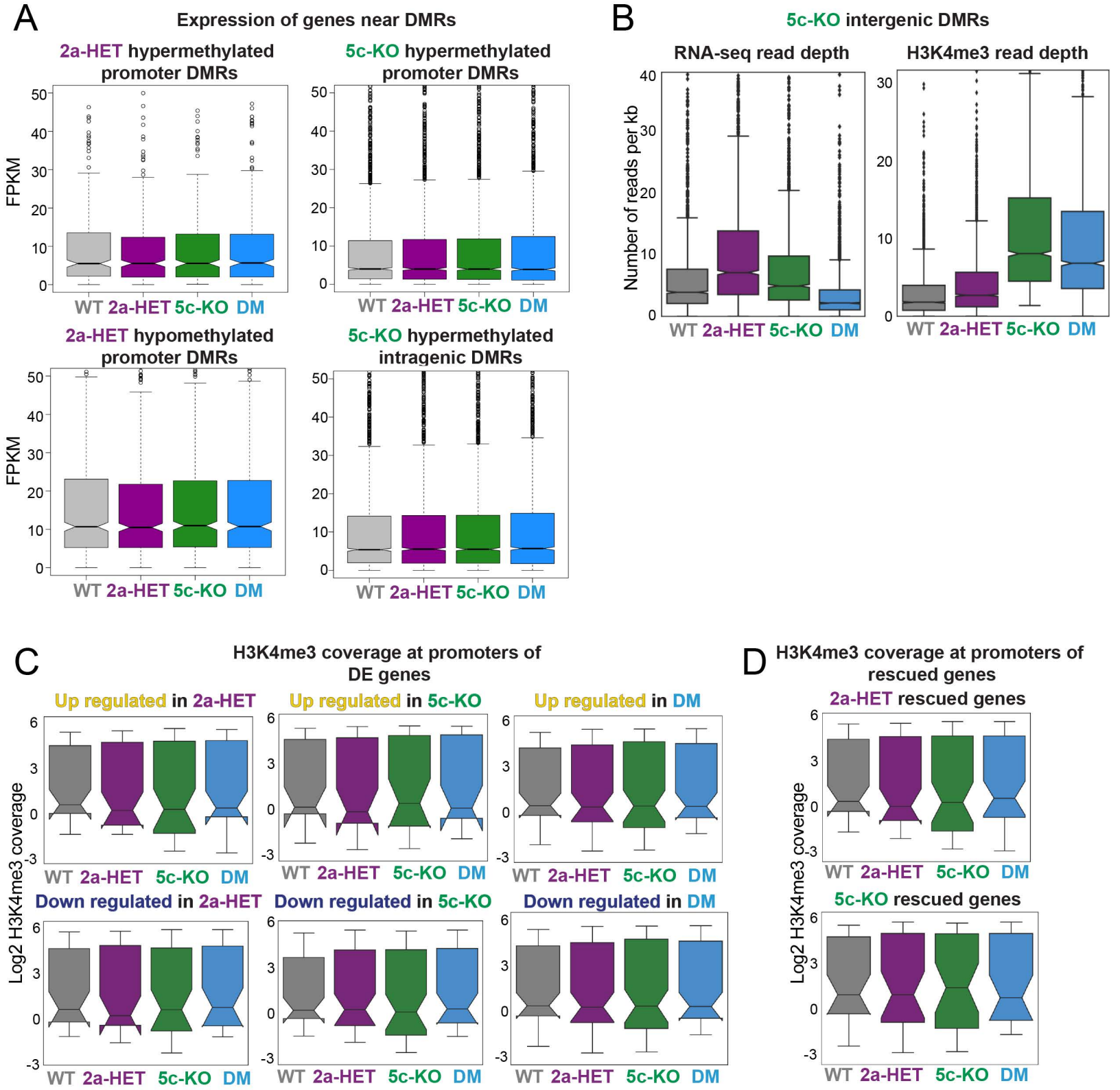

Supplementary Figure 6

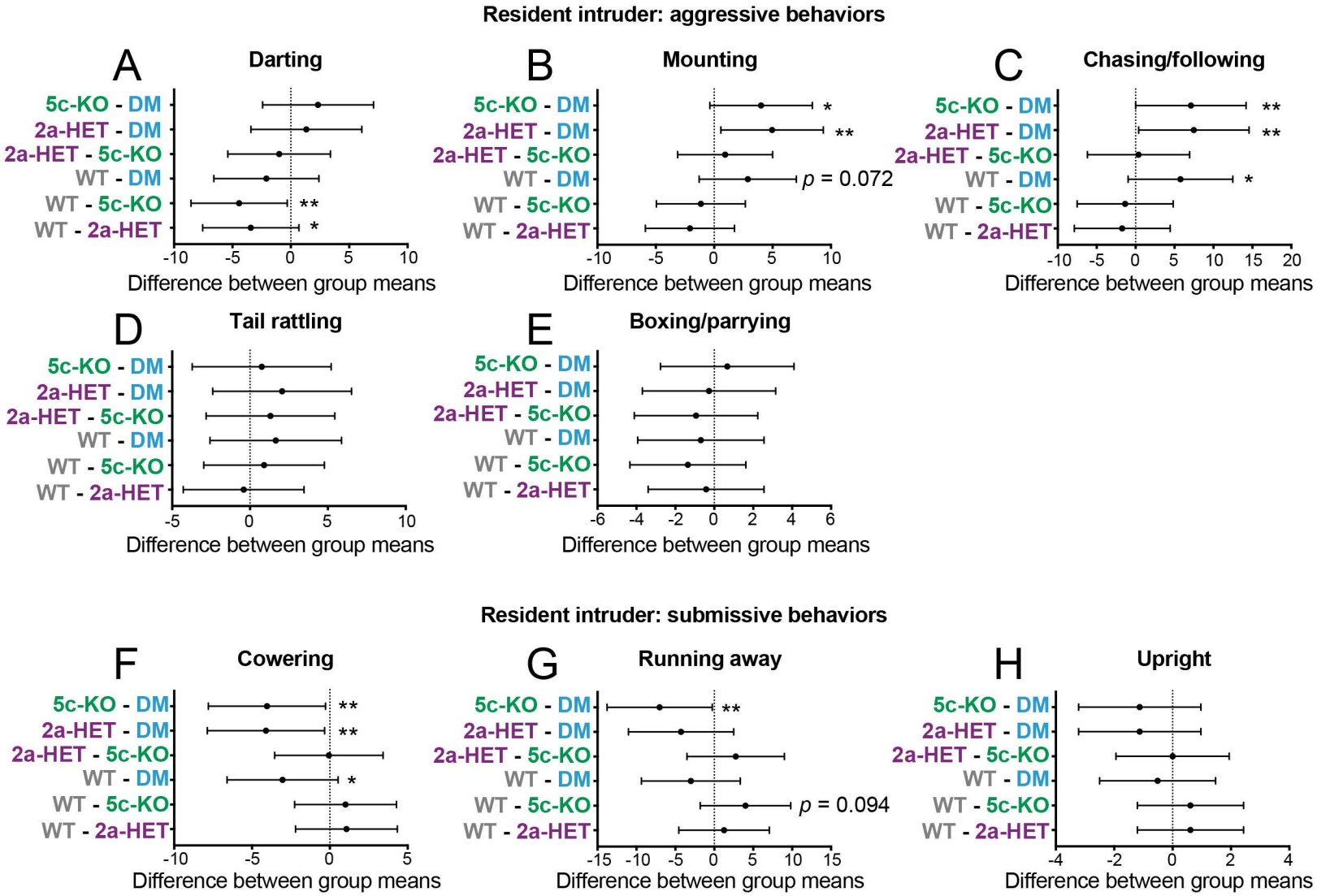

Supplementary Figure 7

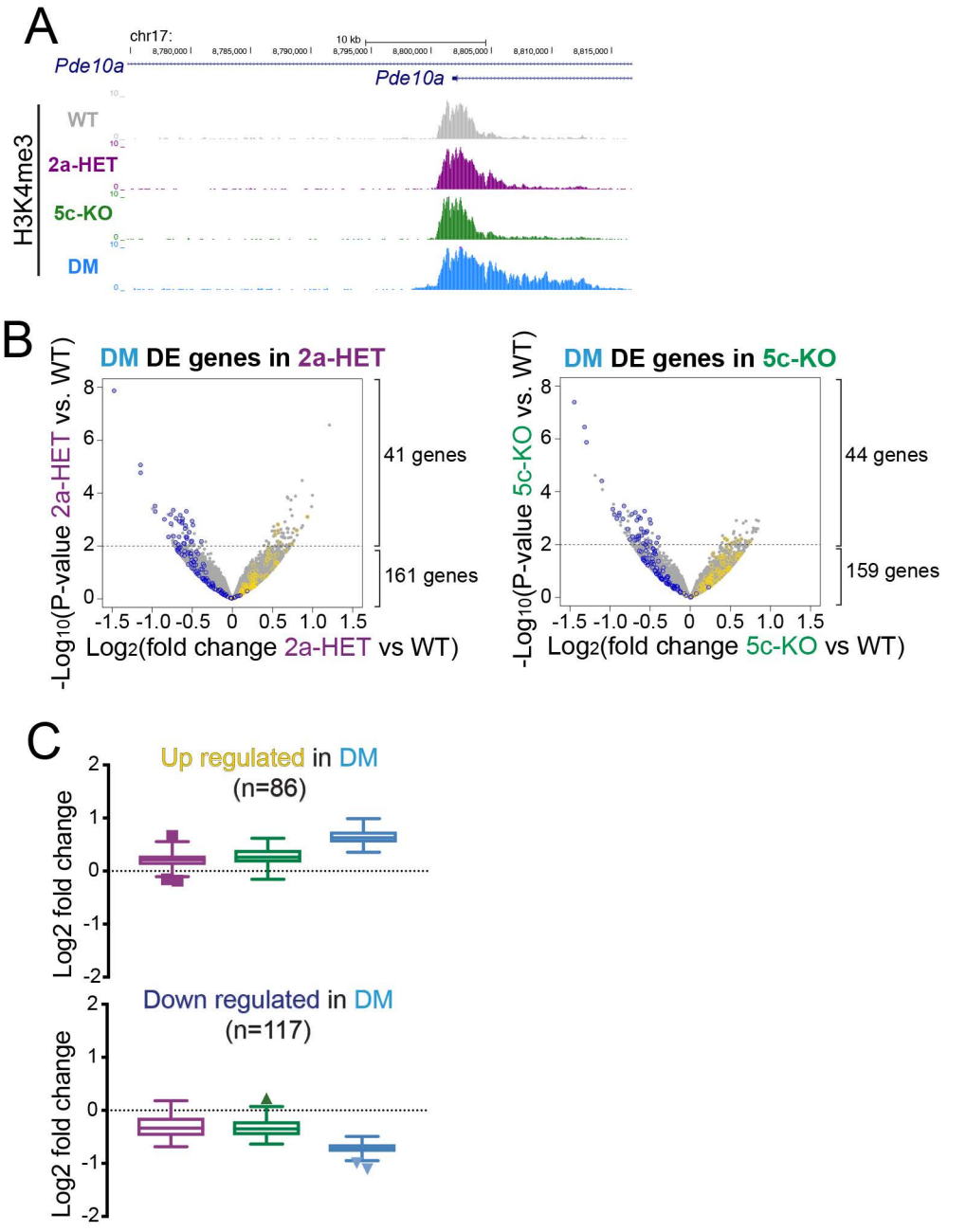

Supplementary Figure 8